Research
A SCIENCE PARTNER JOURNAL

RESEARCH ARTICLE

Multifunctional Hydrogels with Broadband Electromagnetic Interference Shielding and Infrared Stealth Performance in Harsh Environments with Low Conductive Filler Content

Wenchong Ouyang[1,2], Lin Mei[3,4], Limin Xu[5], Chengwei Zhao[6], Yu Bai[7], Ziyang Zhao[2], Rongxin Tang[1,2*], Tianzhi Luo[4*], and Zhengwei Wu[8*]

[1]School of Information Engineering, Nanchang University, Nanchang, Jiangxi 330031, China. [2]Institute of Space Science and Technology, Nanchang University, Nanchang, Jiangxi 330031, China [3]School of Nuclear Science and Technology, University of Science and Technology of China, Hefei 230026, China. [4]CAS Key Laboratory of Mechanical Behavior and Design of Materials, Department of Modern Mechanics, CAS Center for Excellence in Complex System Mechanics, University of Science and Technology of China, Hefei 230026, China. [5]Advanced Institute of Photonics Technology, School of Information Engineering, Guangdong University of Technology, Guangzhou 510006, China. [6]Key Laboratory of Information and Structure Efficiency in Extreme Environment, the Ministry of Education of China, Xidian University, Xi'an 710071, China. [7]Experimental Center of Engineering and Materials Sciences, University of Science and Technology of China, Hefei 230026, China. [8]Joint Laboratory of Plasma Application Technology, Institute of Advanced Technology, University of Science and Technology of China, Hefei 230031, China.

*Address correspondence to: rongxint@ncu.edu.cn (R.T.); tzluo@ustc.edu.cn (T.L.); wuzw@ustc.edu.cn (Z.W.)

Citation: Ouyang W, Mei L, Xu L, Zhao C, Bai Y, Zhao Z, Tang R, Luo T, Wu Z. Multifunctional Hydrogels with Broadband Electromagnetic Interference Shielding and Infrared Stealth Performance in Harsh Environments with Low Conductive Filler Content. *Research* 2026;9:Article 1020. https://doi.org/10.34133/research.1020

Submitted 26 September 2025
Revised 1 November 2025
Accepted 5 November 2025
Published 6 February 2026

Copyright © 2026 Wenchong Ouyang et al. Exclusive licensee Science and Technology Review Publishing House. No claim to original U.S. Government Works. Distributed under a Creative Commons Attribution License (CC BY 4.0).

Stretchable conductive hydrogel composites with infrared stealth and electromagnetic interference (EMI) shielding are in high demand for aerospace, military, and soft robotics. However, realizing stable and efficient performance with low conductive filler content under harsh conditions remains a substantial challenge. Herein, a flexible multifunctional double network hydrogels with high performance and environmental stability was constructed via transition metal carbide/nitride (MXene)/$(NH_4)_2SO_4$-treated strategy-assisted ultrasonic dispersion and thermal polymerization method. The synergistic effect of MXene and $(NH_4)_2SO_4$ within the hydrogel system led to a 3-fold enhancement in mechanical properties, 20-dB improvement in EMI shielding effectiveness, and 40% enhancement in the gauge factor with only 0.12 wt % conductive filler. Benefiting from its high conductivity, efficient thermal insulation, and composite network structure, the double network hydrogels maintain stable EMI shielding and infrared stealth performance under various harsh conditions including repeated stretching, prolonged water evaporation, low-temperature freezing, high-temperature heating, alcohol lamp flame exposure, and high-strain stretching. These findings demonstrate that the hydrogels combine ultra-low filler efficiency, environmental robustness, and multifunctional adaptability, making it a promising candidate for next-generation aerospace, military, and wearable electronic applications.

Introduction

With the advancement of new-generation industrial technologies such as 5G/6G communications and the Internet of Things, electromagnetic interference (EMI) and radiation pollution have become increasingly severe [1]. This issue significantly impacts the global environment, equipment performance, information security, and human health [2]. The rise of intelligent equipment and the diversification of modern lifestyles have put forward new performance requirements on traditional EMI shielding materials such as sheets, films, and foams, including mechanical toughness, stretchability, and environmental stability, which are crucial for improving the effectiveness, reliability, and cost efficiency of EMI shielding materials [3,4]. Meanwhile, the rapid development of the aerospace and defense industries has introduced new technical requirements for broadband regulation of electromagnetic materials. Broadband electromagnetic control technologies spanning microwave, terahertz, and infrared bands can enhance the

electromagnetic protection and infrared stealth performance, expanding their applicability in complex electromagnetic environments [5,6]. Therefore, there is an urgent demand to develop the multifunctional EMI shielding materials that simultaneously satisfy the demands of ultra-broadband EMI shielding, infrared stealth, high stretchability, excellent mechanical properties, good strain sensing, flame retardant, environmental stability, and cost efficiency.

Conductive hydrogels have attracted extensive attention as next-generation flexible EMI shielding materials due to their tissue-like mechanical properties, high conductivity, and multifunctional stretchability [7,8]. Their unique polymeric network with a high water content enables excellent deformation capacity and high-frequency EMI shielding performance, making them highly suitable for aerospace structural electronics, soft robotics, and stealth applications [9,10]. In recent years, nanomaterials such as graphene, liquid metal, MXene, and metal nanowires have been utilized as conductive fillers in combination with hydrogels that possess water-rich porous structures, thereby achieving flexible, stretchable, and excellent EMI shielding effects [11–14]. Increasing the content of conductive fillers markedly enhances the conductivity and EMI shielding effectiveness (SE) of hydrogels [15–20]. However, this improvement comes at the cost of mechanical properties such as strain, strength, and fracture energy, and high EMI SE relying on large filler loadings significantly raises material cost [19–22]. For instance, doubling the MXene content in MXene/polyvinyl alcohol (PVA) hydrogels can increase EMI SE by over 20 dB, while the strain and stress decreased significantly from 250% to 50% and from 0.14 MPa to 0.04 MPa, respectively [19]. A similar trend was observed in the Poly(potassium thioctate)/PVA/p-MXene, MXene/PAA (polyacrylic acid)–CS (chitosan), and CNC (cellulose nanocrystal)/PAA/liquid metal/MXene hydrogel systems, where increasing the conductive filler concentration greatly enhanced the EMI SE but inevitably led to a decline in strain, strength, and fracture energy [20–23]. Therefore, it is crucial to explore and design strategies to balance excellent mechanical properties and high EMI SE at low conductive content [24], a challenge that has yet to receive sufficient attention. In addition to achieving a desirable balance between mechanical sensing performance and high EMI shielding capability, another critical challenge is to realize broadband electromagnetic regulation. Current EMI SE shielding materials predominantly focus on the microwave band (X-Ka bands) [12–15,17–21,24–29], with limited research on the terahertz band [16,22,23], ultraviolet band [30], and infrared band [31–33]. In aerospace and defense applications, materials capable of broadband electromagnetic regulation across the microwave, terahertz, and infrared ranges are essential for achieving multispectral stealth and reliable signal protection.

Furthermore, the environmental stability of hydrogel-based EMI shielding materials remains underexplored. Hydrogels, with pure water as the primary dispersion medium, inevitably face environmental stability challenges such as water evaporation, freezing at temperatures below 0 °C, and thermal decomposition [34,35]. Additionally, the conductivity and thickness generally decrease during the stretching process [35,36], markedly reducing EMI SE and limiting practical longevity. Although the environmental stability of EMI shielding performance has been extensively studied in films and aerogels [37–40], it remains an area in the initial exploration stage for hydrogel shielding materials. Yu and colleagues [35,41] prepared MXene organic hydrogels and polypyrrole nanotube organic hydrogels using binary solvent systems such as glycerol/H_2O and dimethyl sulfoxide (DMSO)/H_2O, which showed excellent low-temperature resistance and anti-drying properties, maintaining EMI SE values far exceeding the 20-dB commercial standard after 7 d of evaporation and under freezing conditions. Lian and colleagues [15,24] reported that poly-acrylamide-acrylic acid and PEDOT:poly(3,4-ethylenedioxythiophene)/PVA hydrogels retained high EMI SE under strains ranging from 100% to 200%, attributed to the high tensile properties and high conductivity conferred by the hydrogels' base formulation and conductive fillers, respectively. However, there is a notable lack of reports on hydrogel EMI shielding materials that maintain stable high EMI SE under multiple harsh conditions such as high stretchability, low temperatures, and dehydration. Such robustness is essential for expanding the application scope of composite hydrogel EMI shielding materials and enhancing their comprehensive performance. Therefore, achieving excellent EMI shielding performance in the microwave and terahertz ranges, as well as effective infrared shielding, under harsh environments and at low conductive filler contents remains another key challenge in the application of hydrogel EMI shielding materials.

Here, we propose a Ti_3C_2 MXene/$(NH_4)_2SO_4$ treatment strategy to fabricate a multifunctional double network (DN) hydrogels composed of short CS chains and long polyelectrolyte (PE) chains synthesized from acrylic acid (AA) and 2-(dimethylamino) ethyl methacrylate (DMAEMA), which exhibits excellent flexibility, high stretchability, shape adaptability, mechanical sensing, and high EMI SE with environmental stability. Remarkably, the PE-CS hydrogels treated by MXene/$(NH_4)_2SO_4$ (MNSPC) demonstrate significant improvements in both mechanical properties and EMI SE. By further optimizing the ratio of MXene/$(NH_4)_2SO_4$ in the gel, MNSPC DN hydrogels achieve peak tensile strength, modulus, and strain of 1.24 MPa, 0.49 MPa, and 495%, respectively, at an ultra-low MXene content of 0.12 wt %, and exhibit exceptional ultra-wideband EMI shielding across X-band, Ku-band, Ka-band, and THz-band, as well as infrared shielding performance. Moreover, the MNSPC DN hydrogels still maintain stable EMI SE and infrared shielding performance, even under various harsh conditions such as 150% high tensile strain, long-term water evaporation, low-temperature freezing, and flame exposure. These findings provide valuable guidance for the development of low-cost, high-performance, environmentally stable, and stretchable EMI shielding hydrogels, demonstrating strong application potential in flexible electronics, bioelectronics, and smart sensors.

Results

Fabrication and characterization of MNSPC DN hydrogels

MNSPC DN hydrogels were fabricated via ultrasonically assisted dispersion combined with thermal polymerization and salting-out methods, following the process illustrated in Fig. 1A. First, AA, CS, DMAEMA, V-50, Ti_3C_2 MXene suspension, and an appropriate volume of ultrapure water are mixed. The mixture is subjected to ultrasonically assisted dispersion to ensure uniform dispersion, particularly of the MXene, followed by vacuum mixing for degassing. PE networks are then formed using *N*,*N*-methylenebis(acrylamide) (MBAA) as a cross-linker, with polymerization initiated by V-50 at 50 °C for 12 h. Finally, the hydrogels undergo a salting-out process in a $(NH_4)_2SO_4$ solution

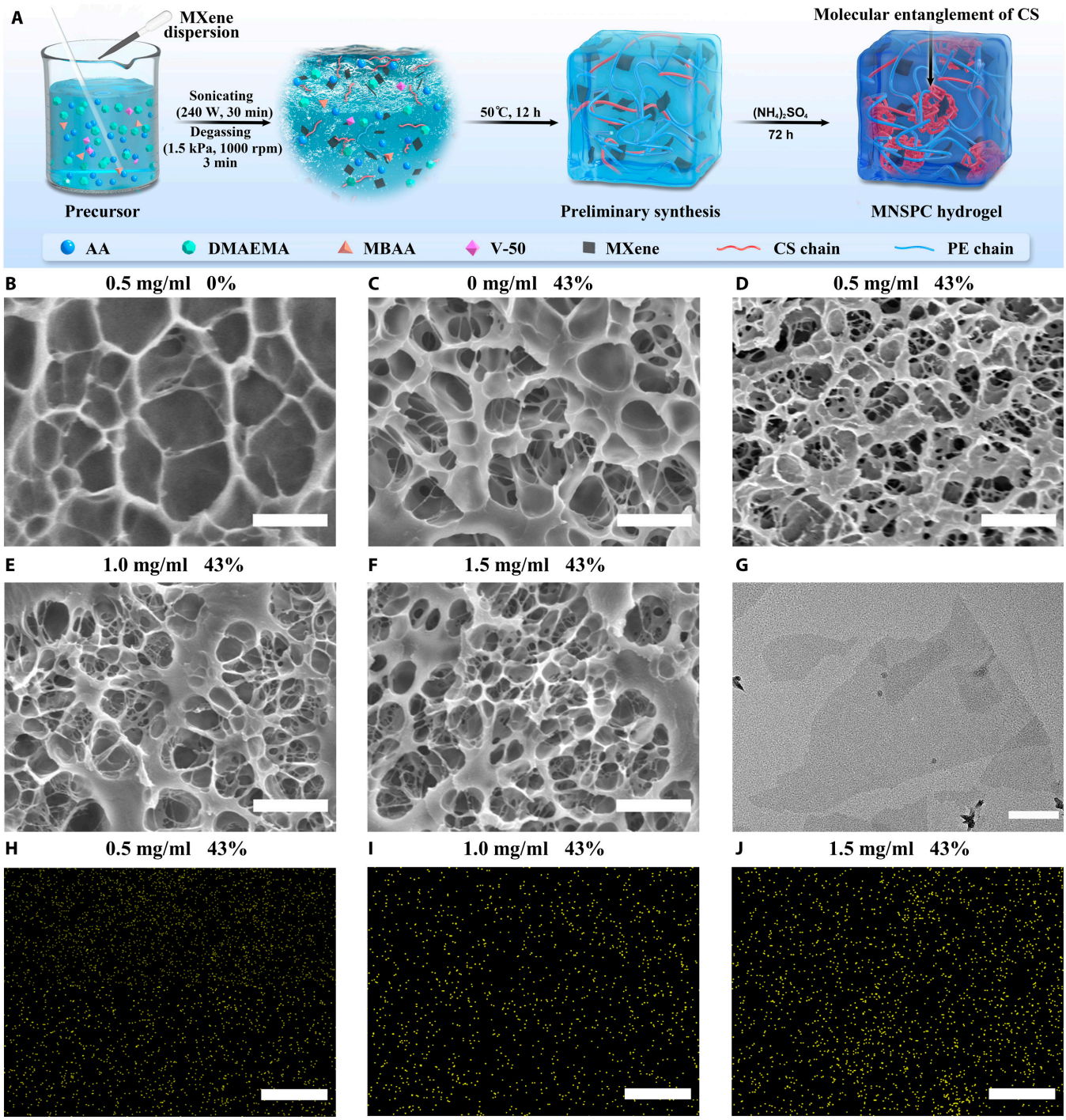


Fig. 1. Fabrication and SEM, TEM, and EDS characterizations of MNSPC DN hydrogels. (A) Fabrication of MNSPC hydrogels. SEM images of hydrogels (B) before salting out (MPC hydrogels with 0.5 mg/ml MXene) and after salting out [MNSPC hydrogels with 43% $(NH_4)_2SO_4$] under different MXene contents: (C) 0 mg/ml MXene [$(NH_4)_2SO_4$/PE-CS (NSPC) hydrogels], (D) 0.5 mg/ml MXene, (E) 1.0 mg/ml MXene, and (F) 1.5 mg/ml MXene [(B) to (F): scale bar, 1 μm]. (G) TEM image of MXene nanosheets (scale bar, 200 nm). EDS mapping of titanium element distribution in MNSPC hydrogels after salting out with (H) 0.5 mg/ml MXene, (I) 1.0 mg/ml MXene, and (J) 1.5 mg/ml MXene [(H) to (J): scale bar, 10 μm].

for 72 h, establishing a CS ionic network and triggering the Hofmeister effect, forming the MNSPC DN hydrogels. Briefly, the random copolymerization of AA and DMAEMA forms the PE chains, while $(NH4)_2SO_4$ induces the formation of the CS ionic network and triggers the Hofmeister effect, leading to molecular entanglement of CS chains. The interaction between MXene and the polymer network constitutes the entire hydrogel system.

Scanning electron microscopy (SEM), transmission electron microscopy (TEM), and energy-dispersive spectroscopy (EDS) characterization results reveal the porosity of hydrogels, formation of the CS ionic network, and uniform dispersion of MXene, respectively (Fig. 1). To minimize the effect of $(NH_4)_2SO_4$ crystallization on the pores and microstructures of the hydrogels in SEM observations (Fig. S1), all samples containing $(NH_4)_2SO_4$

are soaked in deionized water at 30 °C for 30 min before freeze-drying, ensuring more precise visualization of the network structures in the SEM images. SEM analysis of MXene/PE-CS (MPC) and MNSPC hydrogel samples (Fig. 1B and D) clearly demonstrates that the hydrogels exhibit a denser network and smaller pore sizes after salting out (Fig. S2), indicating the formation of the CS ionic network [42]. Similar trends are observed for MNSPC hydrogels with varying $(NH_4)_2SO_4$ concentrations (Fig. S3), where an increase in $(NH_4)_2SO_4$ concentration results in the contraction of the network pore size (Fig. S4). The influence of MXene content on the density of the hydrogel network and pore size after salting out is relatively minimal (Fig. 1C to F). Low concentrations of MXene lead to a slight reduction in pore size, while higher concentrations of MXene increase pore size (Fig. S5). The pore size of the hydrogels not only plays a crucial role in mechanical properties such as strength and toughness but also significantly affects the dispersion of MXene and its synergistic interactions [23,43]. TEM analysis reveals that the average length of MXene nanosheets is approximately 500 nm (Fig. 1G), which is smaller than the pore sizes of the hydrogels. This suggests that the pore structure provides a suitable environment for the efficient dispersion of MXene within the hydrogel matrix and the formation of conductive networks. EDS results further confirm that MXene can still be uniformly dispersed in the MNSPC DN hydrogels after high-concentration $(NH_4)_2SO_4$ salting out (Fig. 1H to J and Fig. S6).

X-ray diffraction (XRD), Fourier transform infrared (FTIR), Raman spectra, and x-ray photoelectron spectra (XPS) characterization experiments were performed to confirm the successful synthesis of MNSPC DN hydrogels, and to further explore the interactions between MXene, PE chains, CS chains, and $(NH_4)_2SO_4$ within the hydrogel system. In the XRD characterization results, MNSPC, NSPC, and PC hydrogels exhibited similar peak profiles. The characteristic diffraction peak of MXene (002) in MNSPC shifted from 6.94° to 6.46°, indicating the successful integration of MXene, PE chains, and CS chains into the hydrogel structure (Fig. 2A) [16]. Compared to the PC hydrogel, the MNSPC (20.26°, 22.86°, 33.70°) and NSPC (16.82°, 20.26°, 33.70°, 51.54°) hydrogels displayed characteristic peaks consistent with $(NH_4)_2SO_4$ (Fig. S7), demonstrating the successful incorporation of $(NH_4)_2SO_4$ into the hydrogel structure. However, slight differences in the peak positions of the characteristic peaks shared with $(NH_4)_2SO_4$ were observed in MNSPC and NSPC hydrogels, which could be attributed to the synergistic interactions between MXene, $(NH_4)_2SO_4$, and the polymer network (PE and CS chains). In the Raman spectra, the MNSPC hydrogels exhibited characteristic peaks corresponding to MXene at approximately 210.13, 357.51, and 734.26 cm^{-1}, associated with the A_{1g}(Ti, C, O), E_g, and A_{1g}(C) modes (Fig. 2B). Compared to the PC hydrogels, both MNSPC and NSPC hydrogels exhibited several characteristic peaks of $(NH_4)_2SO_4$ at 627.08 and 976.54 cm^{-1}. Furthermore, in the MNSPC hydrogel, the A_{1g}(C) peak of MXene shifted from 723.63 to 734.26 cm^{-1}, suggesting potential interactions between MXene and the PE and CS chains [22,23]. FTIR analysis results revealed a shift in the −OH peak of the MNSPC hydrogels from 3,185.93 cm^{-1} in the NSPC hydrogels to 3,195.95 cm^{-1} (Fig. 2C), suggesting that the titanium-abundant surface groups of MXene facilitate the formation of additional hydrogen bonds [16,24]. The C=O peak in the NSPC hydrogels shifted from 1,698.02 cm^{-1} in the PC hydrogels to 1,716.82 cm^{-1}, with a noticeable change in peak morphology, which can be attributed to the complex interactions between $(NH_4)_2SO_4$ and the polymeric network. Compared to the NSPC hydrogels, the MNSPC hydrogels exhibited a significantly stronger and broader peak near 1,701.39 cm^{-1}, which may be attributed to the C=O stretching vibrations of the oxygen-containing functional groups on the MXene surface [24]. Additionally, similar peak features to those of the NSPC and PC hydrogels at approximately 1,413.57 and 1,079.46 cm^{-1} were observed in the MNSPC hydrogels.

In the XPS spectra results, the coexistence of C 1s, N 1s, O 1s, S 2p, Ti 2p, and F 1s was observed in the MNSPC composite hydrogels. However, Ti 2p and F 1s were not detected in the NSPC hydrogels, and Ti 2p, F 1s, and S 2p were absent in the PC hydrogels, confirming the successful incorporation of MXene, PE chains, CS chains, and $(NH_4)_2SO_4$ in the MNSPC hydrogel (Fig. 2D). The deconvolution of C 1s, O 1s, N 1s, S 2p, and Ti 2p peaks was performed to explore the interactions within the MNSPC DN hydrogel system. The C 1s spectrum showed peaks at 281.9, 284.8, 286.2, and 288.8 eV, corresponding to C–Ti–O, C–C, C–O/C–N, and C=O, respectively (Fig. 2E) [44]. The O 1s spectrum presented 2 main peaks at 531.9 and 534.0 eV, which can be attributed to Ti–O and O–H, respectively (Fig. 2F) [21,23]. Ti 2p spectrum exhibited 4 pairs of Ti $2p_{3/2}$ and Ti $2p_{1/2}$ doublets at 455.3/461.5 eV (Ti–C), 456.4/462.3 eV (Ti^{2+}), 457.2/462.8 eV (Ti^{3+}), and 458.6/464.8 eV (Ti–O) (Fig. 2G) [23,44]. S 2p spectrum showed 2 pairs of S $2p_{3/2}$ and S $2p_{1/2}$ doublets at 163.8/165.0 eV and 168.4/169.6 eV, corresponding to C–S and SO_4^{2-}, respectively (Fig. 2H) [22]. The existence of SO_4^{2-} in the S 2p spectrum further confirms the successful incorporation of $(NH_4)_2SO_4$ into MNSPC hydrogels. The N 1s XPS results showed that the peaks were located at 399.6, 401.65, and 401.86 eV, corresponding to -NH-, $-NH_2$, and NH_4^+ in the MNSPC hydrogels (Fig. 2I) [22,44]. AA and DMAEMA were randomly copolymerized to form PE chains, and $-COO^-$ in AA and $-NH_3^+$ in DMAEMA [45] were randomly distributed on the PE chains. $-NH_2$ in CS will be protonated in an acidic environment to form $-NH_3^+$ [46], and these $-NH_3^+$ groups can also combine with $-COO^-$ on the PE chain to form ionic bonds [47]. The ionic bonds established by Coulomb interactions between inter-chain and intra-chain groups with different charges, along with the molecular entanglement of CS chains induced by the Hofmeister effect from $(NH_4)_2SO_4$ (Fig. 1B to F), significantly enhanced the mechanical properties of the hydrogel [22]. The above characterization results further confirmed the successful synthesis and interaction of PE, CS, MXene, and $(NH_4)_2SO_4$ in the MNSPC DN hydrogels.

Mechanical properties

MNSPC hydrogels can withstand various deformations, including but not limited to stretching, knotting, and twisting, as well as lifting a 1-kg weight that is more than 1,000 times its own weight (Fig. 3A), while maintaining excellent shape adaptability (Fig. 3B). These phenomena revealed the superior mechanical properties of MNSPC DN hydrogels. The MXene/$(NH_4)_2SO_4$ treatment strategy significantly enhances the mechanical properties of hydrogels, and the mechanical performance of the MNSPC DN hydrogels can be precisely modulated through the MXene/$(NH_4)_2SO_4$ ratio.

To explore the regulation pattern of MXene/$(NH_4)_2SO_4$ concentrations on mechanical properties and the synergistic enhancement mechanism, the effects of MXene content, $(NH_4)_2SO_4$

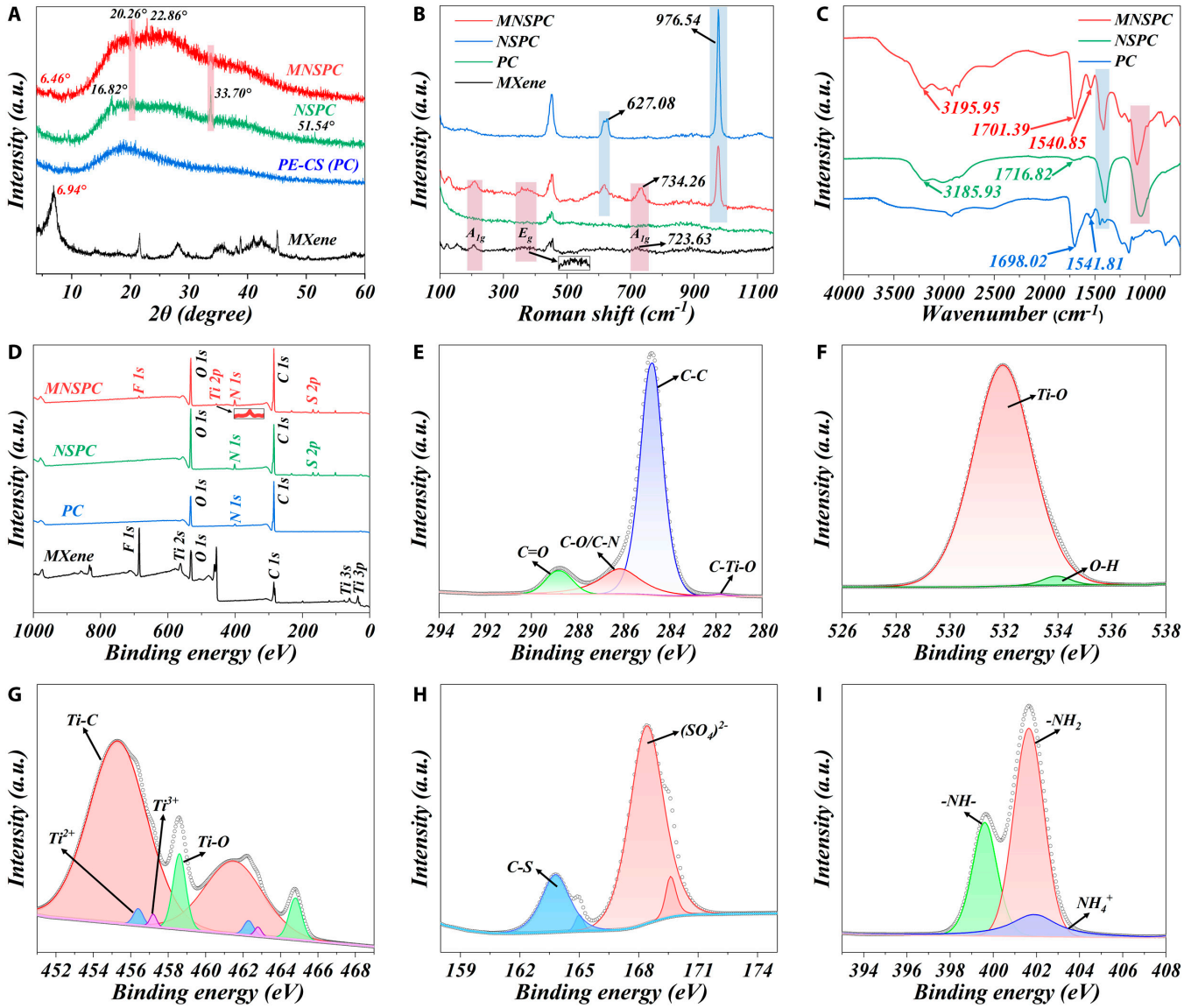


Fig. 2. Comparison of characterization experimental results of MNSPC DN hydrogels and different reference samples. (A) XRD spectrum, (B) Raman spectra, (C) FTIR spectra, (D) XPS, and (E to I) high-resolution spectra of (E) C 1s, (F) O 1s, (G) S 2p, (H) Ti 2p, and (I) N 1s for MNSPC hydrogels.

content, and the MXene/$(NH_4)_2SO_4$ ratio on the tensile strength, modulus, strain, and toughness were systematically analyzed (Fig. 3C to J). A small MXene content (from 0 to 0.5 mg/ml) slightly increased the strength, modulus, maximum strain, and toughness of hydrogels. However, with the continuous rise of MXene content to 1.5 mg/ml, the strength of MPC hydrogels decreases from 0.35 to 0.30 MPa, the modulus drops from 0.15 to 0.10 MPa (Fig. 3C and D), and the toughness declines from 0.92 to 0.88 MJ/m^3 (Fig. 3E). The maximum strain of MPC hydrogels increases monotonically from 436% to 664% with increasing MXene contents (Fig. 3C and E). Overall, the increase in MXene conductive filler tends to reduce the comprehensive mechanical properties of MPC hydrogels, and similar phenomena have also been observed in studies by other researchers [20–24].

The further introduction of $(NH_4)_2SO_4$ into the MPC hydrogels (forming MNSPC hydrogels) significantly enhances their mechanical properties, with the strengthening effect far surpassing that of MXene. As the concentration of $(NH_4)_2SO_4$ increases from 0% to 43%, the strength of MNSPC DN hydrogels increases from 0.35 to 1.77 MPa, the modulus from 0.13 to 0.56 MPa (Fig. 3F and G), and the toughness from 0.78 to 3.74 MJ/m^3 (Fig. 3H). This remarkable improvement in mechanical performance is attributed to the formation of a DN and the strengthening of first network by the increase in the density of ionic bonds. The denser network structure and smaller pore sizes observed in the SEM images of the MPC hydrogels treated with $(NH_4)_2SO_4$ (MNSPC) provide additional support for this explanation (Fig. 1B to D). Additionally, the Hofmeister effect induced by $(NH_4)_2SO_4$ enhances the molecular entanglement of CS chains, promoting the self-entanglement of the CS network and its interpenetration with the PE network [48,49]. Clearly, compared with PC and MPC hydrogels, the MXene/$(NH_4)_2SO_4$-treated hydrogels (MNSPC) exhibited a 3-fold increase in strength, modulus, and toughness, along with about 120% slight improvement in maximum strain (Fig. 3I). Although the NSPC hydrogel also demonstrates a significant improvement in overall mechanical properties, its strain-stretching performance is notably inferior to that of the MNSPC hydrogels, which is critical for the development of stretchable hydrogel shielding materials.

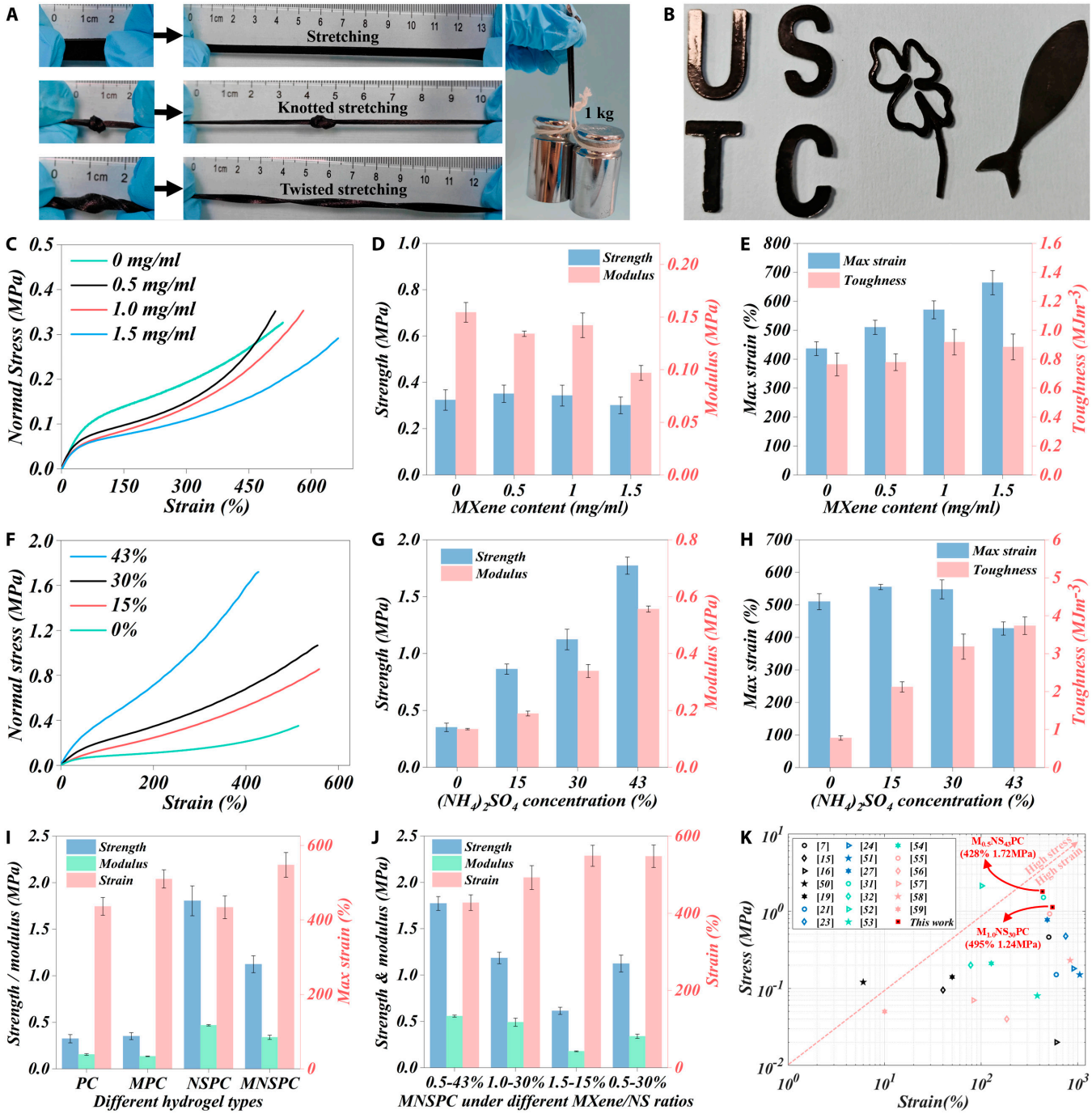


Fig. 3. Mechanical properties of MNSPC DN hydrogels. (A) Stretching, knotting stretching, twisting stretching, and lifting a weight of 1 kg. (B) Shape adaptability, influence of MXene contents on the (C) stress–strain curves, (D) tensile strength and modulus, and (E) tensile strain and toughness of MPC hydrogels [$(NH_4)_2SO_4$: 0]. Effect of $(NH_4)_2SO_4$ contents on the (F) stress–strain curves, (G) tensile strength and modulus, and (H) tensile strain and toughness of MNSPC hydrogels (MXene: 0.5 mg/ml). Comparison of comprehensive mechanical properties of MNSPC hydrogels under (I) different hydrogel types and (J) different MXene/$(NH_4)_2SO_4$ ratios. (K) Comparison of comprehensive mechanical properties between MNSPC hydrogels and representative EMI shielding hydrogels.

Notably, the maximum strain of MNSPC increases from 510% to 548% as the concentration of $(NH_4)_2SO_4$ rises from 0% to 30%, but significantly decreases to 427% when $(NH_4)_2SO_4$ content reaches saturation at 43% (Fig. 3F and H). Excessive ions formed by excessive salting out lead to excessive cross-linking and inhomogeneity between polymer chains, thus forming a denser but less flexible network structure, which is reflected in the larger error bars observed in the mechanical performance results of high-concentration $(NH_4)_2SO_4$ hydrogels (Fig. 3G and H and Fig. S8). Although this dense structure improves the rigidity of the hydrogel, it may also limit its elasticity and cause a decrease in strain capacity. On the other hand, the salting-out effect induced by excessive ammonium sulfate renders the hydrogel denser and less swellable, thereby limiting its stretchability. Additionally, the influence of MXene content observed in MNSPC hydrogels differed significantly from that in MPC hydrogels,

suggesting a potential synergistic interaction between $(NH_4)_2SO_4$ and MXene.

Therefore, a further investigation of the synergistic effects between MXene and $(NH_4)_2SO_4$ content is essential for dynamically controlling the mechanical properties of MNSPC hydrogels and achieving optimal performance. The results of MNSPC hydrogels with varying MXene content at a high-concentration $(NH_4)_2SO_4$ of 43% indicated that the overall mechanical properties were minimally influenced by MXene, despite slight increases in strain and toughness as the increasing MXene content (Fig. S8A to C). However, this impact was nearly negligible relative to the excellent overall performance. Analysis of MNSPC hydrogels with 1.5 mg/ml MXene under different $(NH_4)_2SO_4$ concentrations revealed a significant increase in strength, modulus, and toughness with the rise in $(NH_4)_2SO_4$, accompanied by a consistent decrease in strain (Fig. S8D to F). Although the strength, modulus, and toughness reached their highest values at a concentration of 43% $(NH_4)_2SO_4$, the more critical stretchability was reduced to 433%. A similar pattern was observed in hydrogels with lower MXene content (0.5 mg/ml), where strain initially increased with rising $(NH_4)_2SO_4$ contents but exhibited a marked decrease at the higher 43% concentration (Fig. 3F to H). Based on the trends observed under high $(NH_4)_2SO_4$ concentrations (43%) with varying MXene content, as well as under different $(NH_4)_2SO_4$ concentrations with both high (1.5 mg/ml) and low (0.5 mg/ml) MXene contents (Fig. 3 and Fig. S8), and considering strain stretchability as the primary performance criterion, $M_{0.5}NS_{43}PC$, $M_{1.0}NS_{43}PC$, $M_{1.5}NS_{15}PC$, and $M_{0.5}NS_{30}PC$ were selected for further comparison to explore the optimal MXene/$(NH_4)_2SO_4$ ratio. Notably, $M_{0.5}NS_{30}PC$ hydrogels exhibited the highest stretchability at 548% with the lowest MXene content (0.5mg/ml), although its strength and modulus were slightly lower than $M_{0.5}NS_{43}PC$ and $M_{1.0}NS_{43}PC$ hydrogels, still achieving excellent values of 1.12 MPa (strength) and 0.34 MPa (modulus), respectively (Fig. 3J).

Overall, the strength, modulus, toughness, and strain of hydrogels treated with the MXene/$(NH_4)_2SO_4$ strategy were significantly enhanced. The MNSPC hydrogels with an optimal ratio of 1.0 mg/ml MXene and 30% $(NH_4)_2SO_4$ ($M_{1.0}NS_{30}PC$) achieved exceptional mechanical performance, with strain, strength, modulus, and toughness reaching 495%, 1.24 MPa, 0.49 MPa, and 3.19 MJm^{-3}, surpassing most hydrogel shielding materials reported so far (Fig. 3K and Table S1) [7,15,16,19,21,23,24,27,31,32,50–59].

Strain sensitivity sensor properties

The MNSPC hydrogel exhibited significant potential in deformation sensing applications due to its excellent conductivity (Fig. S9) [19–23]. The gauge factor (GF) was measured to assess the influence of MXene and $(NH_4)_2SO_4$ on the strain sensor properties of the MNSPC hydrogel. The incorporation of MXene led to a marked increase in GF. However, only a slight decrease was observed with further increases in MXene concentration, with the maximum GF occurring at a concentration of 1 mg/ml (Fig. 4A and B). Conversely, the introduction of $(NH_4)_2SO_4$ resulted in a significant reduction in GF, with a progressive decline as the $(NH_4)_2SO_4$ concentration increased (Fig. 4C and D). Similar trends were observed when comparing the GF results across different hydrogel types. MPC hydrogels exhibited higher GF values than did PC hydrogels, while NSPC hydrogels showed lower GF values (Fig. 4E and F). However, the MNSPC hydrogel exhibited a distinctly higher GF than other hydrogels (Fig. 4E and F), attributed to the synergistic effect of MXene and ammonium sulfate, which optimally balanced both conductivity and mechanical properties (Fig. 3 and Fig. S9). Notably, in the higher strain range (200% to 400%), the maximum GF reached 8.47 ± 0.71, surpassing most reported EMI shielding materials (Table S2) [3,35,52,60–80].

In addition, the stability and repeatability of the sensor are critical for practical applications. The changes in resistance under different strain cycles demonstrated the excellent reproducibility and stability of the MNSPC hydrogel sensor (Fig. 4G and H). The practical feasibility of the MNSPC hydrogel sensor was further validated by integrating the hydrogel with a light-emitting diode (LED) and applying it to various body parts. The brightness of the LED significantly decreased as the hydrogel was stretched, owing to the increased resistance from the stretching, which reduced the current in the circuit (Fig. S10). The MNSPC hydrogel sensor effectively monitored finger bending and wrist rotation at different angles, with significant changes in the GF indicating its superior sensitivity (Fig. 4I and J). The sensor also detected facial movements, showing distinct resistance changes when words such as "Alpha" and "Banana" were spoken (Fig. 4K). Moreover, real-time resistance responses showed notable differences when a balloon was compressed at different speeds (Fig. 4L). The above results on stability, repeatability, and practical demonstrations confirm that the MNSPC hydrogel can be an excellent candidate for next-generation flexible strain sensors.

Ultra-broadband EMI shielding performance and environmental stability

Conductive hydrogels are promising candidates for flexible EMI shielding materials due to their porous structure, hydrophilic environments, and high conductivity [19,20]. The MXene/$(NH_4)_2SO_4$ treatment strategy alters the microstructure of MNSPC DN hydrogels and enhances their conductivity, which is crucial for improving EMI shielding performance [21–26].

Test results of the dynamic microwave and terahertz time-domain spectroscopy (THz-TDS) system reveal that the EMI SE of MPC hydrogels significantly increases across the X-band to the THz-band with the rising content of MXene (Fig. 5A and Fig. S11), and the enhancement effect of MXene in the THz-band is slightly higher than that in low-frequency bands such as the X-band (Fig. 5B). The enhancement in EMI SE is attributed to the increased conductivity induced by MXene (Fig. S9A), which effectively promotes the formation of a conductive network. The introduction of $(NH_4)_2SO_4$ further elevates the EMI SE of NSPC hydrogels, significantly surpassing that of PC hydrogels. However, with the increase of $(NH_4)_2SO_4$ concentrations, the EMI SE of NSPC hydrogels exhibits a nonmonotonic trend, initially increasing and then decreasing (Fig. 5C and Fig. S12). The maximum EMI SE enhancement, ranging from 13.6 to 16.9 dB across different frequency bands, is observed at a 30% $(NH_4)_2SO_4$ concentrations (Fig. 5D). This behavior arises from the sharp conductivity increase induced by $(NH_4)_2SO_4$ concentration, with the highest conductivity corresponding to the optimal EMI SE at this concentration (Fig. S9B). Notably, a substantially stronger influence is observed for $(NH_4)_2SO_4$ content relative to MXene (Fig. 5B and D). This effect originates from its superior conductivity, ionic polarization effects, and excellent dispersion and uniformity of $(NH_4)_2SO_4$ (Fig. S11A and B), which avoids issues such as layer stacking and local uniformity of MXene, especially in broadband applications.

The synergistic treatment of MNSPC hydrogels with MXene/$(NH_4)_2SO_4$ produced an EMI SE enhancement exceeding 20 dB, markedly greater than that achieved by either MXene or $(NH_4)_2SO_4$

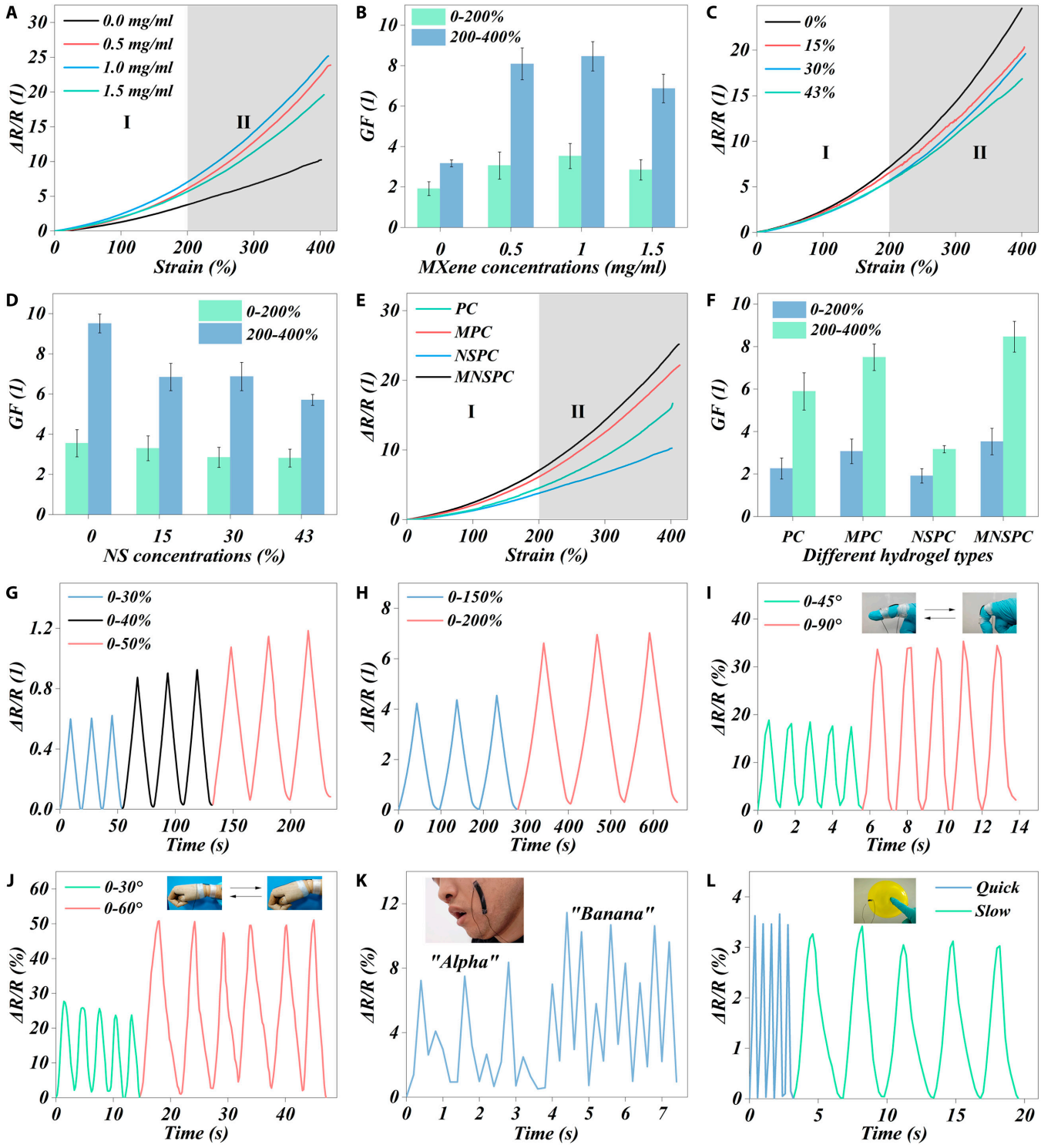


Fig. 4. Strain sensitivity sensor properties and stability of MNSPC hydrogel under different component concentrations. (A) Relative resistance–strain curves and (B) GF in the range of 0% to 200% and 200% to 400% of MNSPC hydrogels with different MXene contents. (C) Relative resistance–strain curves and (D) GF in the range of 0% to 200% and 200% to 400% of MNSPC hydrogels with different $(NH_4)_2SO_4$ contents. (E) Relative resistance–strain curves and (F) GF in the range of 0% to 200% and 200% to 400% of MNSPC hydrogels under different hydrogel types. Real-time $\Delta R/R$ curves recorded during cycles under (G) lower strain and (H) higher strain. Real-time $\Delta R/R$ curves of (I) finger grasping and (J) wrist rotation under different angles, (K) facial movement of speaking different words, and (L) balloon under pressure at different speeds.

component alone (Fig. 5E and F). Although both MXene and $(NH_4)_2SO_4$ individually contribute to improved EMI shielding performance, excessive concentrations lead to a decrease in EMI SE. Additionally, the relative proportions of MXene and $(NH_4)_2SO_4$ significantly affect their synergistic effect. For instance, a significant decline in EMI SE is observed as $(NH_4)_2SO_4$ concentration increases from 30% to saturation with 43% (Fig. 5C and D). Thus, optimizing the MXene/$(NH_4)_2SO_4$ ratio is critical for achieving

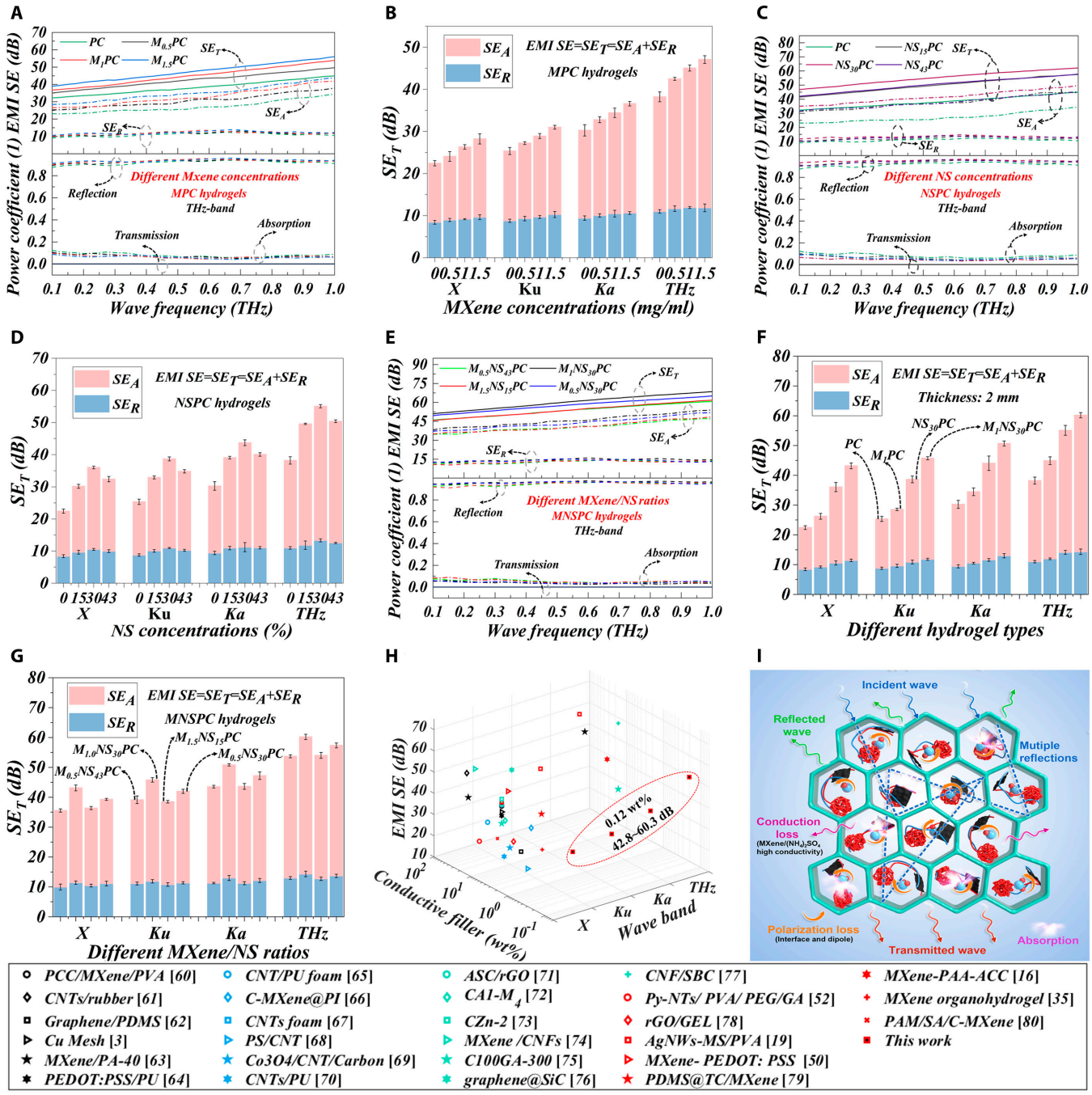


Fig. 5. EMI shielding performance and related mechanism analysis of MNSPC DN hydrogels under different conditions. (A) EMI SE and power coefficient in THz-band across various MXene concentrations. (B) Influence analysis of MXene on EMI SE in different wave bands. (C) EMI SE and power coefficient in THz-band across various $(NH_4)_2SO_4$ concentrations. (D) Influence analysis of $(NH_4)_2SO_4$ concentrations on EMI SE in different wave bands. (E) EMI SE and power coefficient in THz-band under various MXene/$(NH_4)_2SO_4$ ratios. Comparison of SE_R, SE_A, and SE_T in different wave bands under (F) different hydrogel types and (G) MXene/$(NH_4)_2SO_4$ ratios. (H) Comparison of EMI SE under conductive fillers. (I) Analysis of EMI shielding mechanism.

high EMI SE and mechanical performance with minimal conductive filler content. EMI SE and power coefficient under different MXene/$(NH_4)_2SO_4$ ratios were further systematically analyzed, including high MXene with 1.5 mg/ml and low $(NH_4)_2SO_4$ with 15% ($M_{1.5}NS_{15}PC$), low MXene with 0.5 mg/ml and high $(NH_4)_2SO_4$ with 43% ($M_{0.5}NS_{43}PC$), and moderate MXene with 1.0 mg/ml and moderate $(NH_4)_2SO_4$ with 30% ($M_{1.0}NS_{30}PC$). The $M_{1.0}NS_{30}PC$ hydrogel exhibits higher SE_R and SE_A contributions than do $M_{1.5}NS_{15}PC$ and $M_{0.5}NS_{43}PC$ hydrogels, resulting in higher EMI SE (Fig. 5E and G and Fig. S13). This improvement can be attributed to the optimal balance between electronic and ionic conductivity, polarization effects, and conductive loss achieved with moderate concentrations of MXene and $(NH_4)_2SO_4$, providing the best EMI shielding performance. Further increasing $(NH_4)_2SO_4$ content leads to excessive ion concentration, causing the conductivity to decrease (Fig. S9B). On the other hand, the influence of MXene content on EMI shielding performance is significantly less than that of $(NH_4)_2SO_4$, and high MXene content

cannot compensate for the negative impact of low $(NH_4)_2SO_4$ on EMI SE (Fig. 5A to G). Considering the goal of minimizing MXene filler content to reduce cost, the EMI SE of $M_{1.0}NS_{30}PC$ hydrogel at the optimal MXene/$(NH_4)_2SO_4$ ratio achieved EMI SE values of 43.1 dB in X-band, 45.8 dB in Ku-band, 50.8 dB in Ka-band, and 60.3 dB in THz-band (Fig. 5G). Notably, MNSPC DN hydrogel achieved high-performance EMI shielding across broadband (exceeding 60 dB in the THz-band) with a shallow MXene filler content of 0.12 wt %, representing the lowest conductive filler loading reported to date among flexible MXene-based hydrogel EMI shielding materials (Fig. 5H and Table S2).

The power reflection and absorption coefficients of MNSPC DN hydrogels vary depending on the MXene and $(NH_4)_2SO_4$ contents. However, the sum of the power reflection and absorption coefficients remains nearly equal to 1, indicating that the EMI shielding mechanism of MNSPC DN hydrogels is contributed by absorption and reflection effects (Fig. 5I). The specific shielding mechanism is illustrated in Fig. 5I. First, the presence of water molecules within the hydrogel facilitates energy dissipation and enhances wave absorption, while its porous network extends the propagation pathways and promotes multiple internal reflections and absorption [11]. MXene treatment significantly enhances the conductivity of the hydrogel (Fig. S9A), forming a conductive MXene network that boosts conduction losses. Combined with polarization effects of MXene, the CS chain and the PE chain markedly enhance the EMI SE [12]. Further treatment with $(NH_4)_2SO_4$ introduces NH_4^+ and SO_4^{2-} ions, which significantly increase the conductivity of MNSPC hydrogels (Fig. S13B and C), contributing to the conduction losses [13]. Additionally, higher ion concentration intensifies the ionic polarization effect under an electric field, resulting in better absorption and scattering of electromagnetic energy within the material, achieving an approximate 20-dB enhancement in EMI SE.

The harsh working environment poses a considerable challenge to the actual SE and stability of EMI shielding materials. EMI shielding effect test results and videos involving devices such as computers and high-voltage power supplies visually demonstrate the excellent EMI shielding effect of MNSPC hydrogels (Fig. 6A and B and Movie S1). The electric field intensity, as high as 866 V/m from the high-voltage power supply (Fig. 6A) and 72 V/m from the computer (Fig. 6B), is instantaneously reduced to zero upon being shielded by MNSPC hydrogels. Benefiting from the mechanical robustness and flexibility of the MNSPC hydrogel, the EMI SE remains virtually unaffected after over 1,000 cycles of repeated stretching and bending (Fig. 6C). In practical applications, hydrogel shielding materials inevitably experience long-term water evaporation. The EMI SE of MNSPC hydrogels in the terahertz band decreased to 35.6 dB after 5 d and then remained stable (Fig. 6D). Notably, the MNSPC hydrogel demonstrated excellent stability as an organic hydrogel under water evaporation conditions and was significantly superior to traditional MXene hydrogels (Fig. 6D). In view of the extreme working conditions of certain electronic devices, such as low-temperature freezing and high-temperature heating, the EMI SE was measured before and after exposure to −30 °C freezing and 150 °C heating for various durations. After freezing at −30 °C for 5 h, the EMI SE decreased from 60.3 dB to 44.3 dB but recovered to over 60 dB upon thawing (Fig. 6E). This recovery is due to the temporary disruption of the conductive network caused by ice formation during freezing, which does not result in permanent damage (Fig. S14). A similar decrease in EMI SE was observed after heating at 150 °C, with the EMI SE dropping to 32.5 dB after 60 s of heating (Fig. 6F). High temperatures primarily lead to water evaporation, which affects the internal structure of the hydrogel. Yet, it does not reach the decomposition temperature of the MXene or $(NH_4)_2SO_4$ components (Fig. S14). However, the reduction in EMI SE under alcohol burner flame exposure (down to 24.9 dB) was much more pronounced than at 150 °C heating environment (Fig. 6G), because the inner and outer flame temperatures of the alcohol burner exceed 500 °C, leading to the rapid evaporation of water from the hydrogel and the decrease in conductivity (Fig. S14). Moreover, the elevated temperature causes decomposition of the hydrogel matrix components, resulting in structural damage to the hydrogel system. The EMI SE results under varying strain levels demonstrated the advantages of MNSPC hydrogels in practical shielding applications. Even under a significant strain of 150%, the EMI SE in the terahertz band remained at 38.2 dB (with a shielding efficiency exceeding 99%) (Fig. 6H), surpassing that of most reported conductive EMI materials [20,24,81–86]. Moreover, this performance was achieved with an ultra-low conductive filler content of 0.12 wt % (Fig. 5H).

Clearly, under extreme conditions such as water evaporation, low-temperature freezing, flame exposure, high-temperature heating, and tensile strain, the MNSPC hydrogel exhibited varying degrees of reduction in EMI SE (Fig. 6I). Nevertheless, due to its conductivity in the range of 0.06 to 3.58 S/m (Fig. S14), it continues to demonstrate an EMI SE exceeding 20 dB under different harsh environments, which surpasses the commercial application threshold. This highlights the significant potential of MNSPC hydrogels for EMI shielding applications under harsh environmental conditions and complex structural requirements.

Infrared stealth performance and environmental stability

Infrared sensors easily detect objects with temperatures above absolute zero due to continuous thermal radiation. The infrared stealth properties of MNSPC hydrogels with 2-mm thickness were evaluated using a thermal imaging camera, which is crucial for expanding their potential applications in aerospace and military fields. The radiation temperature of the hand area covered by MNSPC hydrogel decreased from 34.9 °C to 19.5 °C compared to an infrared target, demonstrating a temperature distribution similar to that of the surrounding environment, thereby providing direct evidence for excellent infrared stealth performance of the MNSPC hydrogel (Fig. 7A). Compared with PC, MPC, and NSPC hydrogels, the MNSPC hydrogel treated with the MXene/$(NH_4)_2SO_4$ strategy exhibited significantly improved infrared stealth, arising from the synergistic role of the MXene conductive network for electromagnetic to thermal energy conversion and the structural changes in the hydrogel induced by $(NH_4)_2SO_4$ (Figs. S3 and S9).

Infrared stealth materials inevitably encounter harsh working environments in practical applications, and their exceptional environmental stability is critical for expanding their application scenarios and enhancing market competitiveness. Hydrogels face the inevitable issue of prolonged water evaporation in practical applications due to the dependence on their water-rich environment. The infrared stealth performance of the MNSPC hydrogel decreased after water evaporation (the radiation temperature of covered hydrogel increased from 24.1 °C to 25.6 °C). However, even after 7 d of prolonged water evaporation, the infrared target temperature decreased from 36.3 °C to 25.6 °C,

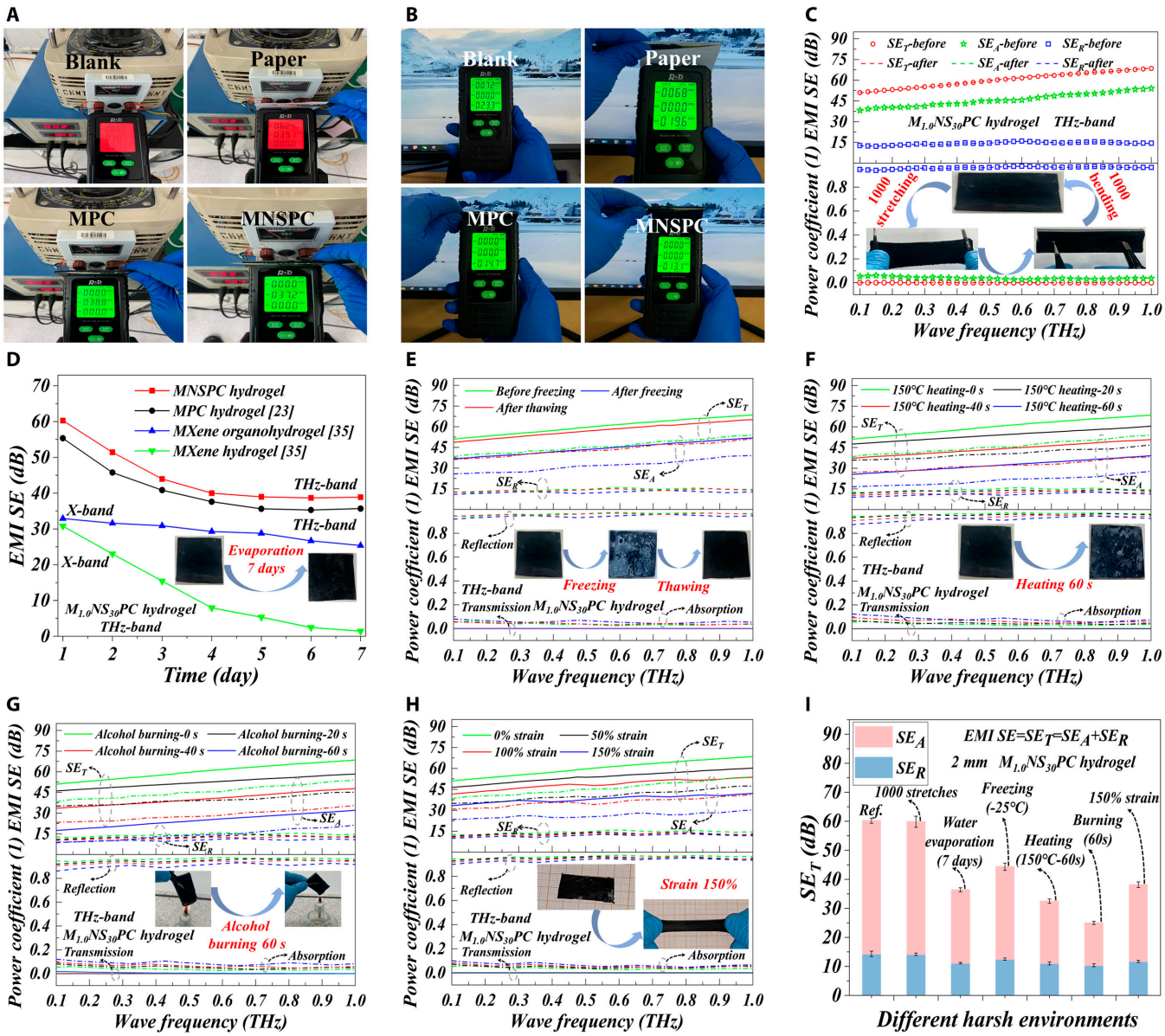


Fig. 6. Practical application effect and environmental stability of MNSPC hydrogels in different harsh environments. Demonstrations of practical shielding effect of MNSPC hydrogel on (A) power supply and (B) computer. Effect of (C) repeated stretching and bending for 1,000 cycles, (D) water evaporation over 7 d, (E) low-temperature freezing at −30 °C over 5 h, (F) heating at 150 °C, (G) flame burning, and (H) stretching under different strain levels. (I) Comparative analysis of different environments effects on the EMI SE of MNSPC hydrogels.

still exhibiting excellent infrared stealth (Fig. 7B). Under a low-temperature environment of −30 °C, the hydrogel underwent freezing, yet the frozen MNSPC hydrogel continued to show good infrared stealth performance, and almost unaffected by the increase in freezing time (Fig. 7C). After exposure to the alcohol lamp flame for 60 s, significant degradation in infrared stealth of MNSPC hydrogels was observed due to the water evaporation and structural degradation of the hydrogel caused by the flame temperature exceeding 500 °C. However, when rehydrated in a water-rich environment for 20 s, the infrared stealth performance was restored (Fig. 7D). Interestingly, under 150% tensile strain, a marked increase in infrared shielding performance was observed, with the radiation temperature of the MNSPC hydrogel-covered area decreasing from 23.6 °C to 16.9 °C (Fig. 7E). This phenomenon can be attributed to the enhanced infrared scattering and absorption effects caused by the increased propagation path and the increased structural nonuniformity of MNSPC hydrogels.

Furthermore, the infrared stealth and thermal insulation properties of the MNSPC hydrogel were tested under high-temperature conditions using a constant-temperature heating platform. Under a high-temperature environment of 150 °C, the temperature of MNSPC hydrogel gradually rose from 33.6 °C to 79.1 °C within 60 s (Fig. 7F). Compared to the infrared target at 150 °C, the radiation temperature of the hydrogel-covered area decreased by approximately 70.9 °C, demonstrating excellent thermal insulation performance and stability (Fig. 7G). Although infrared stealth performance showed varying

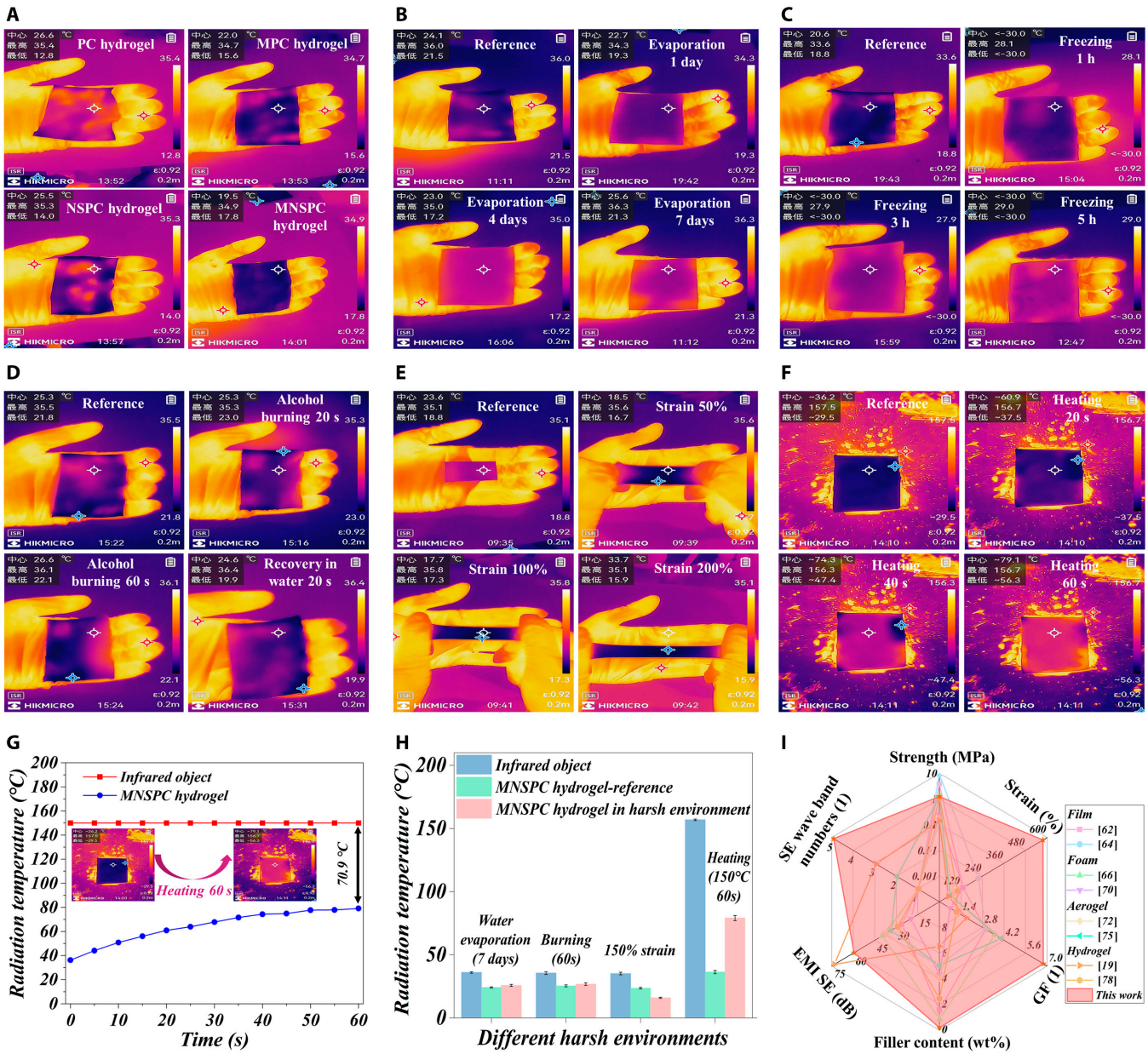


Fig. 7. Infrared stealth performance environmental stability of MNSPC hydrogels in different harsh environments. (A) Infrared stealth performance of different hydrogel types. Effect of harsh environments such as (B) water evaporation, (C) low-temperature freezing, (D) flame burning, (E) stretching under different strain levels, and (F) high-temperature heating on the infrared stealth performance of MNSPC hydrogels. (G) Radiation temperature curves of MNSPC hydrogels on the thermal stages of 150 °C. (H) Comparison of radiation temperature of MNSPC hydrogels under different harsh environments. (I) Comparison of comprehensive performance between MNSPC hydrogel and typical EMI shielding materials.

degrees of change in different harsh environments, including water evaporation, low-temperature freezing, flame burning, high-strain stretching, and high-temperature heating, it still maintained excellent infrared stealth (Fig. 7H). Compared with typical shielding materials such as films, foams, aerogels, and hydrogels, the comprehensive performance of MNSPC hydrogels ranks among the best (Figs. 3K, 5H, and 7I).

Discussion

In summary, an MNSPC DN hydrogel with strong mechanical sensing, stable high EMI shielding, and infrared stealth performance under various harsh working environments has been designed and produced using MXene/$(NH_4)_2SO_4$-treated strategy-assisted ultrasonic dispersion and thermal polymerization method. $(NH_4)_2SO_4$ triggered the Hofmeister effect and induced molecular entanglement of CS within the hydrogel, resulting in about 3-fold enhancement in mechanical properties. The MXene nanosheets were induced to align orderly the porous network structure in the hydrogel, forming a continuous MXene conductive pathway, in synergy with $(NH_4)_2SO_4$ to significantly enhance the conductivity. The MXene/$(NH_4)_2SO_4$ synergistic effect enables the MNSPC DN hydrogel to achieve excellent mechanical properties (strain with 495%, strength with 1.24 MPa, modulus with 0.49 MPa, and toughness with 3.19 MJ·m^{-3}), ultra-wideband high-performance EMI shielding across the X-band, Ka-band,

Ku-band, and THz-band with 60.3 dB, and exceptional infrared stealth performance, with only 0.12 wt % low conductive filler content and a thickness of 2 mm. Meanwhile, benefiting from the high conductivity, thermal stability, composite network structure, and excellent mechanical properties of MNSPC DN hydrogels, it still maintained EMI SE well above 20 dB and excellent infrared stealth performance under various harsh conditions such as repeated stretching, prolonged water evaporation, low-temperature freezing, high-temperature heating, flame exposure, and 150% tensile strain. Moreover, the easy processability of the MNSPC DN hydrogels with high GF is of great significance for scalable applications in electronic devices and soft robotics with complex shapes. In short, the MNSPC DN hydrogels with exceptional design and MXene/$(NH_4)_2SO_4$ strategy exhibit great application potential for scalable aerospace, military, soft robotics, and wearable electronic devices for the sake of its excellent mechanical sensing performance, stable EMI shielding and infrared stealth effects resistant to various harsh environments, low cost with 0.12 wt % conductive filler, and easy processability.

Methods

Materials

AA [99%, containing 200 ppm (parts per million) MEHQ as inhibitor], DMAEMA (99%, containing 1,000 ppm MEHQ as inhibitor), 2,2′-azobis(2-methyl-propionamidine) dihydrochloride (V-50,97%), and ammonium sulfate [$(NH_4)_2SO_4$, 99%] were purchased from Aladdin Reagent Co. Ltd., China. MBAA (99%) was purchased from Sigma-Aldrich. Short-chain CS [degree of deacetylation >90%, viscosity 45 mPa·s for 1% (w/v) solution] was purchased from Jinhu Company, China. Ti_3C_2 MXene dispersion was obtained from 11 Technology Co. Ltd., Jilin, China.

Fabrication of DN MNSPC hydrogel

The MNSPC hydrogels were fabricated using the following steps. Firstly, 4 g of AA, 0.5 g of DMAEMA, 0.4 g of CS, 2.5 mg of MBAA, 50 μl of 0.8 M V-50 solution, and varying volumes (0, 0.25, 0.5, and 0.75 ml) of 20 mg/ml MXene dispersion were mixed, and deionized water was added to adjust the total volume of precursor mixture to 10 ml. The mass fraction of MXene can be calculated based on the MXene content per unit volume of hydrogel:

$$(\mathrm{wt\%})(\mathrm{MXene}) = \frac{\rho_M V_H}{M_H} \tag{1}$$

where ρ_M refers to the MXene content per unit volume of hydrogel, and M_H and V_H represent the mass and volume of hydrogel.

This precursor mixture was then sonicated in an ice bath using a SCIENTZ-IID ultrasonic homogenizer (Scientz Biotechnology Co. Ltd., Ningbo) at 240 W for 30 min to ensure uniform dispersion of the MXene. The mixture was degassed using a TMV-200T Vacuum Mixer (Smida Intelligent Equipment Co. Ltd., Shenzhen) at 1.5 kPa and 1,000 rpm for 3 min. Following this, the mixture was injected into a mold composed of 2 glass plates separated by a silicone rubber spacer to obtain hydrogel sheets. The polymerization of the PE chains was initiated at 50 °C for 12 h, with MBAA acting as the cross-linker and V-50 as the thermal initiator. Finally, the MNSPC composite hydrogels underwent salting out in an $(NH_4)_2SO_4$ solution for 72 h to establish the CS ionic network and trigger the Hofmeister effect, resulting in the formation of the MNSPC DN hydrogels.

Materials characterizations

SEM images of the hydrogels and EDS were captured by Gemini SEM 500 (ZEISS, Germany) at accelerating voltages of 10 and 8 kV, respectively. TEM images of the Ti_3C_2 MXene nanosheets were obtained using an HT7700 Exalens (HITACHI, Japan) at an accelerating voltage of 100 kV. Crystallographic data of the samples were recorded using XRD on Theta/Theta Rotating anode X-ray Diffractometer (TTR III, Japan). Raman spectroscopy measurements were performed using the Confocal Raman System-Horiba LabRAM SoLeil (Horiba, Japan) equipped with a 785-nm laser, and the spectra were recorded in the range of 1,500 to 100 cm^{-1}. FTIR of the samples was performed in the range of 4,000 to 500 cm^{-1} on a Nicolet 8700 IR spectrophotometer (Thermo Scientific, USA). XPS measurements were performed on X-ray Photoelectron Spectrometer-Kratos AXIS SUPRA$^+$ (Shimadzu, Japan).

Mechanical test

Mechanical properties were measured by an HY-0350 testing machine (HengYi Instrument Co. Ltd., Shanghai). The samples were stamped into a dumbbell shape with 2-mm inner width, 20-mm gauge length, and 1- to 2-mm thickness for the test. To reduce the effect of dehydration, the tensile rate was set to 50 mm/s. All mechanical properties were tested on no less than 3 samples, average values were selected as the final results, and standard deviations were marked as error bars in the figures.

Strain-sensing test

The samples were cut into a rectangular shape with a width of 6 mm, a thickness of 1 to 2 mm, and a gauge length of 30 mm for the strain-sensing test. The GF was used to quantify the strain sensitivity of the hydrogels. The resistance change of the samples at different strains was measured using a TH2832 LCR meter, while the samples were loaded and unloaded by the finger, wrist, and balloon. The relative changes in stress and resistance determined GF:

$$GF = \frac{R - R_0}{R_0}\frac{1}{\varepsilon - \varepsilon_0} \tag{2}$$

where R_0 and R represent the initial resistance and real-time resistance of the sample, respectively, and ε_0 and ε represent the initial strain and real-time strain of the sample, respectively.

To further demonstrate the functional capability of the hydrogels as sensors, the gels were integrated into a circuit with an LED. Theoretically, stretching the gel would increase its resistance, causing a decrease in the current flowing through the LED, subsequently reducing its brightness.

Electromagnetic shielding test in different EM frequency bands

Electromagnetic shielding bands of hydrogels in this work mainly focus on the X-band (8.2 to 12.4 GHz), Ku-band (12.4 to 18 GHz), Ka-band (90.5 to 40 GHz), and THz-band (0.1 to 1.0 THz). EMI SE values of hydrogels in X-band, Ku-band, and Ka-band were measured by microwave test system (Anritsu-MS46322B vector network analyzer with a range of 1 MHz to 43.5 GHz), and the corresponding samples were cut into a

rectangular shape with 50 mm × 50 mm (length × width) for measurements. The power transmission T_p, reflection R_p, and absorption A_p coefficients in the hydrogels were calculated by S parameters (forward S_{21} and reverse S_{12} transmission coefficients, input S_{22} and output S_{11} reflection coefficients) based on Eqs. (3) to (5), and corresponding EMI SE values of hydrogels were obtained by power transmission and reflection coefficients based on Eqs. (6) to (8).

$$T_p = |S_{12}|^2 = |S_{21}|^2 \tag{3}$$

$$R_p = |S_{11}|^2 = |S_{22}|^2 \tag{4}$$

$$A_p = 1 - T_p - R_p \tag{5}$$

$$EMI\ SE = SE_T = -10\,log\left(T_p\right) \tag{6}$$

$$SE_R = -10\,log\left(\frac{1}{1-R_p}\right) \tag{7}$$

$$SE_A = SE_T - SE_R \tag{8}$$

where SE_T, SE_R, and SE_A represent the overall SE, reflection, and absorption effectiveness (in dB), respectively.

EMI SE values of hydrogels in THz-band were measured using the terahertz time domain spectroscopy (THz-TDS) test system (TAS7400TS). Considering the non-negligible influence of water vapor on terahertz waves, the test environment was controlled below 5% relative humidity (RH) by an air dryer equipped with a temperature and humidity recording transmitter (G95-4PS, Hangzhou Loggertech Co. Ltd.). Overall shielding, reflection, absorption effectiveness, and EMI SE of MPC hydrogels were measured and analyzed in the transmission mode and reflection mode of THz-TDS system based on Eqs. (9) and (10).

$$EMI\ SE = SE_T = -20\,log\left(\frac{E_s}{E_a}\right) \tag{9}$$

$$SE_R = -10\,log\left(\frac{E_r}{E_i}\right) \tag{10}$$

where E_s and E_a refer to the terahertz pulse intensity through MPC hydrogel and air in the transmitted light path, respectively, and E_r and E_i represent the incident and reflected terahertz pulse intensity of hydrogels in reflected optical path, respectively.

Infrared stealth performance test

Infrared stealth performance of hydrogels in this work was tested via infrared thermal camera (H21PROS+, China), with the infrared wavelength range spanning from 8 to 14 μm. The corresponding samples were cut into a rectangular shape with 50 mm × 50 mm (length × width) for measurements. Heating tests in the infrared range were conducted using a stainless steel digital constant-temperature heating plate (LC-DB-AB, China), which generated a 150 °C high-temperature environment while minimizing the influence of surface materials on the infrared measurements.

Statistical analysis

All data were presented as the means ± standard deviation.

Acknowledgments

We are grateful for the technical support from X. Gong, S. Xu, and C. Wang.

Funding: This work was partly supported by the National Natural Science Foundation of China under grant no. 62401534, Young Science and Technology Talent Support Program of Anhui Province Association for Science and Technology under grant no. RCTJ202401, National Natural Science Foundation of China under grant no. 82572440, Joint Laboratory of Plasma Application Technology Funding under grant no. JL06120001H, National Natural Science Foundation of China under grant no. 62401242, and Natural Science Foundation of Jiangxi under grant no. 20224BAB212027.

Author contributions: W.O. and L.M. designed the experiments, analyzed the data, and wrote the manuscript. L.M. and W.O. synthesized and characterized the composite hydrogels. C.Z. helped with part of the EMI SE experiment in the microwave band. L.X. helped with part of the EMI SE experiment in the terahertz band. Y.B. helped with the experiments on materials characterization. W.O., L.M., R.T., L.X., C.Z., Z.Z., T.L., and Z.W. discussed the results and finalized the manuscript. R.T., T.L., and Z.W. supervised the project. All authors discussed the results throughout the project and approved the final version of the manuscript.

Competing interests: The authors declare that they have no competing interests.

Data Availability

Additional data are available from the corresponding author upon request. Data supporting the findings of this study are available within the article and its Supplementary Materials.

Supplementary Materials

Figs. S1 to S14
Tables S1 and S2
Movie S1

References

1. Iqbal A, Shahzad F, Hantanasirisakul K, Kim MK, Kwon J, Hong J, Kim H, Kim D, Gogotsi Y, Koo CM. Anomalous absorption of electromagnetic waves by 2D transition metal carbonitride Ti_3CNT_x (MXene). *Science*. 2020;369(6502):446–450.
2. Cheng JY, Li CB, Xiong YF, Zhang HB, Raza H, Ullah S, Wu JY, Zheng GP, Cao Q, Zhang DQ, et al. Recent advances in design strategies and multifunctionality of flexible electromagnetic interference shielding materials. *Nano-Micro Lett.* 2022;14:80.
3. Chen ZB, Yang SD, Huang JH, Gu YF, Huang WB, Liu SY, Lin ZQ, Zeng ZP, Hu YG, Chen ZM, et al. Flexible, transparent and conductive metal mesh films with ultra-high FoM for stretchable heating and electromagnetic interference shielding. *Nano-Micro Lett*. 2024;16(1):92.
4. Sun Y, Su YT, Chai ZY, Jiang L, Heng LP. Flexible solid-liquid bi-continuous electrically and thermally conductive nanocomposite for electromagnetic interference shielding and heat dissipation. *Nat Commun*. 2024;15(1):7290.

5. Tang XW, Lu YZ, Li SS, Zhu MY, Wang ZX, Li Y, Hu ZY, Zheng PL, Wang ZC, Liu TZ. Hierarchical polyimide nonwoven fabric with ultralow-reflectivity electromagnetic interference shielding and high-temperature resistant infrared stealth performance. *Nano-Micro Lett*. 2025;17(1):82.
6. Liu Q, Wang PL, Zhang W, Mai T, Qi MY, Chen L, Li JF, Ma MG. Multifunctional wood-derived cellulose/$Ti_3C_2T_x$ composite films enhanced by densification strategy for electromagnetic shielding, joule/solar heating, and thermal camouflage. *Chem Eng J*. 2024;493:Article 152696.
7. Guo HT, Shi YY, Pan F, Zheng SH, Chai XL, Yang Y, Jiang HJ, Wang X, Li LX, Zhen X, et al. Tough, stretchable dual-network liquid metal-based hydrogel toward high-performance intelligent on-off electromagnetic interference shielding, human motion detection and self-powered application. *Nano Energy*. 2023;114:Article 108678.
8. Xu GC, No YH, Li HN, Li WL, Lin WT, Xue YR, Li K, Fang Y, Liang HQ, Yang HC, et al. Supergravity-steered generic manufacturing of nanosheets-embedded nanocomposite hydrogel with highly oriented, heterogeneous architecture. *Adv Mater*. 2024;36(24):2400075.
9. Chong JY, Sung CH, Nam KS, Kang TW, Kim H, Lee HS, Park H, Park S, Kang JH. Highly conductive tissue-like hydrogel interface through template-directed assembly. *Nat Commun*. 2023;14(1):2206.
10. He HM, Li H, Pu AY, Li WX, Ban KW, Xu LZ. Hybrid assembly of polymeric nanofiber network for robust and electronically conductive hydrogels. *Nat Commun*. 2023;14(1):759.
11. Zarepour A, Ahmadi S, Rabiee N, Zarrabi A, Iravani S. Self-healing MXene- and graphene-based composites: Properties and applications. *Nano-Micro Lett*. 2023;15(1):100.
12. Zhao B, Bai ZY, Lv HL, Yan ZK, Du YQ, Guo XQ, Zhang JC, Wu LM, Deng JS, Zhang DW, et al. Self-healing liquid metal magnetic hydrogels for smart feedback sensors and high-performance electromagnetic shielding. *Nano-Micro Lett*. 2023;15(1):79.
13. Yang YF, Han MR, Liu W, Wu N, Liu JR. Hydrogel-based composites beyond the porous architectures for electromagnetic interference shielding. *Nano Res*. 2022;15(10):9614–9630.
14. Yan Q, Liu ZL, Xiong JH, Lian HX, Chen H, Fei T, Chen YX, Zheng HW, Zhao X, Xu LL, et al. Stimuli-responsive MXene/PNIPAM hydrogel with high-performance and tunable electromagnetic interference shielding performance. *Adv Sci*. 2025;12(31):Article e05551.
15. Lian YH, Wang HG, Liu LL, Guan L, Lin MM, Li QL, Guo XQ, Liu Z, Chen P, Zhao B, et al. Highly stretchable, transparent hydrogel for electromagnetic interference shielding. *Small Struct*. 2025;6(5):2400486.
16. Zhu YY, Liu J, Guo T, Wang JJ, Tang XZ, Nicolosi V. Multifunctional $Ti_3C_2T_x$ MXene composite hydrogels with strain sensitivity toward absorption-dominated electromagnetic-interference shielding. *ACS Nano*. 2021;15(1):1465–1474.
17. Zhao ZH, Zhang LM, Wu HJ. Hydro/organo/ionogels: "Controllable" electromagnetic wave absorbers. *Adv Mater*. 2022;34(43):2205376.
18. Zhang YF, Li ZH, Xu ZS, Xiao MY, Yuan Y, Jia XL, Shi R, Zhang LQ, Wan PB. Flexible healable electromagnetic-interference-shielding bioelastic hydrogel nanocomposite for machine learning-assisted highly sensitive sensing bioelectrode. *Aggregate*. 2024;5(5):Article e566.
19. Yang YF, Li B, Wu N, Liu W, Zhao SY, Zhang CF, Liu JR, Zeng ZH. Biomimetic porous MXene sediment-based hydrogel for high-performance and multifunctional electromagnetic interference shielding. *ACS Nano*. 2022;16(9):15042–15052.
20. Tian YC, Zhu Y, Qian KP, Miao M, Ye JH, Feng X. Liquid metal integrated cellulose nanocrystal/polyacrylic acid dual-network hydrogel towards high-performance wearable sensing and electromagnetic interference shielding. *J Mater Sci Technol*. 2026;251:124–134.
21. Qian KP, Zhou JY, Miao M, Thaiboonrod S, Fang JH, Feng X. Stretchable supramolecular hydrogel with instantaneous self-healing for electromagnetic interference shielding control and sensing. *Compos Part B Eng*. 2024;287:Article 111826.
22. Mei L, Ouyang WC, Xu LM, Huang YL, Liu Q, Bai Y, Lu QM, Luo TZ, Wu ZW. Super tough multifunctional MXene/PAA-CS double network hydrogels with high mechanical sensing properties and excellent EMI shielding performance. *Small*. 2025;21(6):2410687.
23. Ouyang WC, Mei L, Liu Q, Ding CB, Liu YM, Zhao CW, Xu LM, Lu F, Luo DP, Miao CG, et al. Ultrathin-flexible multifunctional MXene composite hydrogels with good mechanical properties-high strain sensitivity and ultra-broadband EMI shielding performances. *Chem Eng J*. 2024;494:Article 153068.
24. Li P, Wang HN, Ju ZS, Jin ZZ, Ma JG, Yang L, Zhao XN, Xu HY, Liu YC. $Ti_3C_2T_x$ MXene- and sulfuric acid-treated double-network hydrogel with ultralow conductive filler content for stretchable electromagnetic interference shielding. *ACS Nano*. 2024;18(4):2906–2916.
25. Tang JY, Gao Y, Li T, Qin RC, Qi Q, Meng FB. Thermoresistive network in phase-transition hydrogel: Achieving on/off switchable electromagnetic interference shielding. *Adv Funct Mater*. 2025;35(36):2504959.
26. He JZ, Ma ZK, Liu SL, Lu YG, Wu QL. SGs-CNTs/PAM/CCS triple network hydrogel: Neural architecture inspired for broadband EMI shielding and environmental resilience. *Adv Funct Mater*. 2025;35(37):2507404.
27. Fang M, Huang LY, Cui ZR, Yi P, Zou HH, Li XF, Deng G, Chen CY, Geng Z, He JZ, et al. Phase-transition microcapacitor network in organohydrogel for absorption-dominated electromagnetic interference shielding and multi-mode intelligent responsiveness. *Adv Funct Mater*. 2025;35(18):2418870.
28. Zhao R, Liu C, Luo HY, Zhao JW, Zhang JJ, He YY, Li Z, Yang P, Xu L, Wan YF. Nanoengineered injectable hydrogel: An advanced radioprotective barrier with magnetic hyperthermia synergy. *ACS Appl Mater Interfaces*. 2024;16(38):50188–50201.
29. Wang CC, Ding Y, Wu TZ, Li ZH, Hu CS, Wang ZQ, Zhou YH, Lin XY, Zhang WW, Xu JT. Ionic double-network hydrogels for integrated electromagnetic shielding and self-powered sensing in wearable electronics. *Adv Sci*. 2025;12(37):Article e09115.
30. Li L, Liu YF, Zhang HS, Shen HJ, Yin XX, Li HY, Peng HG, Zhou SS, Liu YP, et al. TiO_2-loaded halloysite nanocomposites: Achieving the UV resistance and dielectric stability of polyurea. *Polym Degrad Stab*. 2025;241:Article 111549.
31. Fang JY, Xu J, Zuo PY, Zhou YK, Tang CH, Qian J, Wang RQ, Liu XY, Zhuang QX. New system for green EMI shielding: Organohydrogel with multi-band green electromagnetic shielding, sensing, and infrared-stealth capacity. *J Mater Sci Technol*. 2025;219:1–9.
32. Zhu TY, Jiang WJ, Wu S, Wang Y, Liu YL, Qi XD, Wang Y. Multifunctional MXene/PEDOT:PSS-based phase change

organohydrogels for electromagnetic interference shielding and medium-low temperature infrared stealth. *ACS Appl Mater Interfaces*. 2024;16(12):15372–15382.
33. Wei JS, He P, Yang YT, Tang CX, Long Z, Chen X, Lei TZ, Dai L. Enhancing the electromagnetic interference shielding performance of composite paper with corrugated paper-like structure. *Chem Eng J*. 2024;497:Article 154969.
34. Galib RH, Tian YP, Lei Y, Dang SC, Li XL, Yudhanto A, Lubineau G, Gan QQ. Atmospheric-moisture-induced polyacrylate hydrogels for hybrid passive cooling. *Nat Commun*. 2023;14(1):6707.
35. Yu YH, Yi P, Xu WB, Sun X, Deng G, Liu XF, Shui JL, Yu RH. Environmentally tough and stretchable MXene organohydrogel with exceptionally enhanced electromagnetic interference shielding performances. *Nano-Micro Lett*. 2022;14(1):77.
36. Niu Y, Liu H, He R, Luo M, Shu M, Xu F. Environmentally compatible wearable electronics based on ionically conductive organohydrogels for health monitoring with thermal compatibility, anti-dehydration, and underwater adhesion. *Small*. 2021;17(24):2101151.
37. Cheng Y, Li XY, Qin YX, Fang YT, Liu GL, Wang ZY, Matz J, Dong P, Shen JF, Ye MX. Hierarchically porous polyimide/$Ti_3C_2T_x$ film with stable electromagnetic interference shielding after resisting harsh conditions. *Sci Adv*. 2021;7(39):Article eabj1663.
38. Hassan T, Iqbal A, Yoo B, Jo JY, Cakmakci N, Naqvi SM, Kim H, Jung S, Hussain N, Zafar U, et al. Multifunctional MXene/carbon nanotube janus film for electromagnetic shielding and infrared shielding/detection in harsh environments. *Nano-Micro Lett*. 2024;16:216.
39. Liu N, Li QQ, Wan HJ, Chang LB, Wang H, Fang JH, Ding TP, Wen QY, Zhou LJ, Xiao X. High-temperature stability in air of $Ti_3C_2T_x$ MXene-based composite with extracted bentonite. *Nat Commun*. 2022;14:5551.
40. Sun Y, Han X, Guo P, Chai ZY, Yue JY, Su YT, Tan SD, Sun X, Jiang L, Heng LP. Slippery graphene-bridging liquid metal layered heterostructure nanocomposite for stable high-performance electromagnetic interference shielding. *ACS Nano*. 2023;17(13):12616–12628.
41. Meng LS, Yang S, Ma Y, Zou YP, Zhang Y, Chen G, Dong CJ, Guan HT. Porous polypyrrole nanotube-based organohydrogels: Versatile materials for robust electromagnetic interference shielding in harsh environments. *Chem Eng J*. 2024;479:Article 147643.
42. Yang YY, Wang X, Yang F, Wang LN, Wu DC. Highly elastic and ultratough hybrid ionic–covalent hydrogels with tunable structures and mechanics. *Adv Mater*. 2018;30(18):e1707071.
43. Song YX, Wu HJY, He XT, Fang CL, Song Q, Chen MH, Liu ZR, Lu Y, Yu BR, Liu T, et al. Triboelectric nanogenerator made with stretchable, antibacterial hydrogel electrodes for biomechanical sensing. *ACS Appl Mater Interfaces*. 2024;16(38):50630–50639.
44. Yang L, Fu RZ, Duan ZG, Zhu CH, Fan DD. Artificial nonenzymatic antioxidant MXene nanosheet-anchored injectable hydrogel as a mild photothermal-controlled oxygen release platform for diabetic wound healing. *ACS Nano*. 2022;16(5):7486–7502.
45. Hu Q, Zhang Y, Wang T, Sun W, Tong Z. pH responsive strong polyion complex shape memory hydrogel with spontaneous shape changing and information encryption. *Macromol Rapid Commun*. 2021;42(9):e2000747.
46. Yang JW, Bai RB, Suo ZG. Topological adhesion of wet materials. *Adv Mater*. 2018;30(25):e1800671.
47. Chen JY, Liu FF, Abdiryim T, Yin HY, Liu X. ZnO-$Ti_3C_2T_X$ composites supported on polyacrylic acid/chitosan hydrogels as high-efficiency and recyclable photocatalysts for norfloxacin degradation. *Int J Biol Macromol*. 2024;258:Article 128912.
48. Cong J, Fan ZW, Pan SS, Tian J, Lian WZ, Li S, Wang SJ, Zheng DC, Miao CG, Ding WP, et al. Polyacrylamide/chitosan-based conductive double network hydrogels with outstanding electrical and mechanical performance at low temperatures. *ACS Appl Mater Interfaces*. 2021;13(29):34942–34953.
49. Tang SY, Liu K, Chen JS, Li YZ, Liu MX, Lu L, Zhou CR, Luo BH. Dual-cross-linked liquid crystal hydrogels with controllable viscoelasticity for regulating cell behaviors. *ACS Appl Mater Interfaces*. 2022;14(19):21966–21977.
50. Liu J, Mckeon L, Garcia J, Pinilla S, Barwich S, Möbius M, Stamenov P, Coleman JN, Nicolosi V. Additive manufacturing of Ti3C2-MXene-functionalized conductive polymer hydrogels for electromagnetic-interference shielding. *Adv Mater*. 2022;34:2106253.
51. Huang X, Wang LB, Shen ZH, Ren JF, Chen GX, Li QF, Zhou Z. Super-stretchable and self-healing hydrogel with a three-dimensional silver nanowires network structure for wearable sensor and electromagnetic interference shielding. *Chem Eng J*. 2022;446(2):Article 137136.
52. Lu SQ, Ouyang B, Han SM, Chen K, Wu F, Xie A, Jane AS, Zeng HB. Flexible polypyrrole nanotube-polyethylene glycol-polyvinyl alcohol hydrogel for enhanced electromagnetic shielding. *ACS Appl Nano Mater*. 2022;5(8):11407–11413.
53. Yuan SW, Dai TW, Jiang XY, Zou HW, Liu PB. Transparent and environmentally adaptive semi-interpenetrating network hydrogels for electromagnetic interference shielding. *ACS Appl Nano Mater*. 2023;5(10):8406–8414.
54. Hou MH, Yang SQ, Wang J. Flexible and stretchable hydrogel-based composites using Ag coated hollow glass microspheres and polypyrrole nanotube supported ferroferric oxide for electromagnetic interference shielding. *ACS Appl Nano Mater*. 2024;7(14):16883–16893.
55. Zhao TT, Zhou JY, Wu WT, Qian KP, Zhu Y, Miao M, Feng X. Antibacterial conductive polyacrylamide/quaternary ammonium chitosan hydrogel for electromagnetic interference shielding and strain sensing. *Int J Biol Macromol*. 2024;265:Article 130795.
56. Hu XX, Cheng Y, Wei ZJ, Zhang R, Zhan YH, Xia HS. Enhanced sensing and electromagnetic interference shielding performance of hydrogels by the incorporation of ionic liquids. *ACS Appl Electron Mater*. 2024;6(3):1770–1780.
57. Thi QV, Ryu J, Hong J, Koo CM, Enyi Y, Sohn D, Truong X. pH-tunable 3D interconnected network of multiwalled carbon nanotubes/polyacrylic acid hydrogel with excellent electromagnetic radiation shielding capability. *Adv Mater Technol*. 2024;2024:2401264.
58. Zhang R, Xie D, Zhang CC, Xu ZS, Fang YQ, Wang WH, Xu M, Song YM. A highly stretchable, self-adhesive, anti-freezing, and highly sensitive dual-network conductive hydrogel sensor for multifunctional electronic skin. *J Mater Chem A*. 2023;11(45):24608–24617.
59. Liu J, Garcia J, Leahy LM, Song R, Mullarkey D, Fei B, Dervan A, Shvets IV, Stamenov P, Wang WX. 3D printing of multifunctional conductive polymer composite hydrogels. *Adv Funct Mater*. 2023;33(37):2214196.

60. Guo S, Sheng XX, Li XL, Sheng M, Wu H, Lu X, Qu J. A multifunctional flexible composite film with excellent multi-source driven thermal management, electromagnetic interference shielding, and fire safety performance, inspired by a "brick–mortar" sandwich structure. *Adv Funct Mater*. 2022;32(26):2200570.
61. Jia LC, Li MZ, Yan DX, Cui CH, Wu HY, Li ZM. A strong and tough polymer-carbon nanotube film for flexible and efficient electromagnetic interference shielding. *J Mater Chem C*. 2017;5(35):8944–8951.
62. Wang Z, Yang W, Liu R, Zhang X, Nie H, Liu Y. Highly stretchable graphene/polydimethylsiloxane composite lattices with tailored structure for strain-tolerant EMI shielding performance. *Compos Sci Technol*. 2021;206:Article 108652.
63. Cheng Z, Cao YS, Wang RF, Liu X, Fan F, Huang Y. Multifunctional MXene-based composite films with simultaneous terahertz/gigahertz wave shielding performance for future 6G communication. *J Mater Chem A*. 2023;11:5593–5605.
64. Li P, Du D, Guo L, Guo Y, Ouyang J. Stretchable and conductive polymer films for high-performance electromagnetic interference shielding. *J Mater Chem C*. 2016;4(27):6525–6532.
65. Xu Z, Chen J, Shen B, Zhao Y, Zheng W. A proof-of-concept study of auxetic composite foams with negative poisson's ratio for enhanced strain-stable performance of electromagnetic shielding. *ACS Mater Lett*. 2023;5(2):421–428.
66. Zeng ZH, Wu N, Wei JJ, Yang YF, Wu TT, Li B, Hauser SB, Yang WD, Liu JR, Zhao SY. Porous and ultra-flexible crosslinked MXene/polyimide composites for multifunctional electromagnetic interference shielding. *Nano-Micro Lett*. 2022;14:59.
67. Jia LC, Yan DX, Yang Y, Zhou D, Cui CH, Bianco E, Lou J, Vajtai R, Li B, Ajayan PM, et al. High strain tolerant EMI shielding using carbon nanotube network stabilized rubber composite. *Adv Mater Technol*. 2017;2(7):1700078.
68. Xie YP, Li Z, Tang JH, Li P, Chen W, Liu P, Li L, Zheng Z. Microwave-assisted foaming and sintering to prepare lightweight high-strength polystyrene/carbon nanotube composite foams with an ultralow percolation threshold. *J Mater Chem C*. 2021;9:9702.
69. Liu HG, Zhu ZL, Tian N, Li Y, You C, Islam SM. Synergistically-enhanced flexible electromagnetic interference shielding nanocomposites. *Appl Surf Sci*. 2023;628:Article 157379.
70. Huang K, Chen M, He G, Hu X, He W, Zhou X, Huang Y, Liu Z. Stretchable microwave absorbing and electromagnetic interference shielding foam with hierarchical buckling induced by solvent swelling. *Carbon*. 2020;157:466–477.
71. Wang L, Shi XT, Zhang JL, Zhang Y, Gu J. Lightweight and robust rGO/sugarcane derived hybrid carbon foams with outstanding EMI shielding performance. *J Mater Sci Technol*. 2020;52:119–126.
72. Zhang XX, Qian KP, Fang JH, Thaiboonrod S, Miao M, Feng X. Synchronous deprotonation–protonation for mechanically robust chitin/aramid nanofibers conductive aerogel with excellent pressure sensing, thermal management, and electromagnetic interference shielding. *Nano Res*. 2024;17:2038–2049.
73. Ma H, Wang ZG, Zhang XF, Yao J. Bimetallic MOF@bacterial cellulose derived carbon aerogel for efficient electromagnetic wave absorption. *Ceram Int*. 2023;49(12):20951–20959.
74. Ma C, Mai T, Wang PL, Guo WY, Ma MG. Flexible MXene/nanocellulose composite aerogel film with cellular structure for electromagnetic interference shielding and photothermal conversion. *ACS Appl Mater Interfaces*. 2023;15(40):47425–47433.
75. Cao YS, Cheng Z, Wang RF, Liu X, Zhang T, Fan F, Huang Y. Multifunctional graphene/carbon fiber aerogels toward compatible electromagnetic wave absorption and shielding in gigahertz and terahertz bands with optimized radar cross section. *Carbon*. 2022;199:333–346.
76. Jiang Y, Chen Y, Liu YJ, Sui GX. Lightweight spongy bone-like graphene@SiC aerogel composites for high-performance microwave absorption. *Chem Eng J*. 2018;337:522–531.
77. Pai AR, Lu YZ, Joseph S, Santhosh NM, Degl'Innocenti R, Lin H, Letizia R, Paoloni C, Thomas S. Ultra-broadband shielding of cellulose nanofiber commingled biocarbon functional constructs: A paradigm shift towards sustainable terahertz absorbers. *Chem Eng J*. 2023;467:Article 143213.
78. Yin R, Zhang C, Chen YY, Wang Y, Feng Q, Liu Y, Yu M, Yuan Y, Xu CY, Liu F, et al. Transient, printable and recyclable gelatin hydrogels with enhanced mechanical sensing and electromagnetic shielding performance by incorporation of reduced graphene oxide. *Chem Eng J*. 2023;475:Article 145794.
79. Wei JS, Dai L, Xi XJ, Chen Z, Zhu M, Dong C, Sing S, Lei T. Robust, ultrathin and flexible electromagnetic interference shielding paper designed with all-polysaccharide hydrogel and MXene. *Carbohydr Polym*. 2024;323:Article 121447.
80. Xia BH, Li T, Chen MQ, Wang S, Dong W. L-citrulline-modified Ti3C2Tx MXene nanosheets embedded in polyacrylamide/sodium alginate hydrogels for electromagnetic interference shielding. *ACS Appl Nano Mater*. 2022;5(12):18664–18669.
81. Wang H, Jiang Y, Ma Z, Shi Y, Zhu Y, Huang R, Feng Y, Wang Z, Hong M, Gao J, et al. Hyperplastic, robust, fire-safe multifunctional MXene aerogels with unprece-dented electromagnetic interference shielding efficiency. *Adv Funct Mater*. 2023;33(49):2306884.
82. Liao SY, Li G, Wang XY, Wan YJ, Zhu PL, Hu YG, Zhao T, Sun R, Wong CP. Metallized skeleton of polymer foam based on metal-organic decomposition for high-performance EMI shielding. *ACS Appl Mater Interfaces*. 2022;14(2):3302–3314.
83. Zhang N, Wang Z, Song R, Wang Q, Chen H, Zhang B, Lv H, Wu Z, He D. Flexible and transparent graphene/silver-nanowires composite film for high electromagnetic interference shielding effectiveness. *Sci Bull*. 2019;64(8):540–546.
84. Chen K, Liu M, Shi Y, Wang H, Fu L, Feng Y, Song P. Multi-hierarchical flexible composites towards superior fire safety and electromagnetic interference shielding. *Nano Res*. 2022;15(10):9531–9543.
85. Wei J, Lin Z, Lei Z, Xu Y, Zhao Z, Zhao T, Hu Y, Miao H, Sun R. Lightweight and highly compressible expandable polymer microsphere/silver nanowire composites for wideband electromagnetic interference shielding. *ACS Appl Mater Interfaces*. 2022;14(4):5940–5950.
86. Li B, Yang Y, Wu N, Zhao S, Jin H, Wang G, Li X, Liu W, Liu J, Zeng Z. Bicontinuous, high-strength, and multifunctional chemical-cross-linked MXene/superaligned carbon nanotube film. *ACS Nano*. 2022;16(11):19293–19304.